Check for updates

ADVANCING EARTH AND SPACE SCIENCE

JGR Solid Earth

RESEARCH ARTICLE
10.1029/2022JB025008

The Redox State of Incipient Oceanic Subduction Zones: An Example From the Troodos Ophiolite (Cyprus)

Wen-Jun Hu[1,2,3], Mei-Fu Zhou[1,2], Julia M. Ribeiro[4], John Malpas[3], Ya-Dong Wu[5], and Zhong-Jie Bai[2]

[1]School of Earth Resources, China University of Geosciences, Wuhan, China, [2]State Key Laboratory of Ore Deposit Geochemistry, Institute of Geochemistry, Chinese Academy of Sciences, Guiyang, China, [3]Department of Earth Sciences, The University of Hong Kong, Hong Kong, China, [4]State Key Laboratory of Isotope Geochemistry, Guangzhou Institute of Geochemistry, Chinese Academy of Science, Guangzhou, China, [5]State Key Laboratory of Lithospheric Evolution, Institute of Geology and Geophysics, Chinese Academy of Sciences, Beijing, China

Key Points:

- Percolation of boninitic magmas raised the oxygen fugacity of the Troodos mantle peridotites to a limited extent
- The primary boninitic magmas of the Troodos ophiolite may not be more oxidized than mid-ocean ridge basalts
- The oxidation processes of the Troodos proto-arc mantle may be different from those of the Izu-Bonin-Mariana proto-arc mantle

Supporting Information:

Supporting Information may be found in the online version of this article.

Correspondence to:

M.-F. Zhou,
zhoumeifu@hotmail.com

Citation:

Hu, W.-J., Zhou, M.-F., Ribeiro, J. M., Malpas, J., Wu, Y.-D., & Bai, Z.-J. (2023). The redox state of incipient oceanic subduction zones: An example from the Troodos ophiolite (Cyprus). *Journal of Geophysical Research: Solid Earth*, *128*, e2022JB025008. https://doi.org/10.1029/2022JB025008

Received 27 JUN 2022
Accepted 1 NOV 2022

Author Contributions:

Conceptualization: Wen-Jun Hu, Mei-Fu Zhou, Ya-Dong Wu, Zhong-Jie Bai
Formal analysis: Wen-Jun Hu
Funding acquisition: Mei-Fu Zhou
Investigation: Wen-Jun Hu, John Malpas
Methodology: Ya-Dong Wu
Project Administration: Mei-Fu Zhou
Resources: Mei-Fu Zhou, John Malpas
Software: Ya-Dong Wu
Supervision: Mei-Fu Zhou
Writing – original draft: Wen-Jun Hu
Writing – review & editing: Wen-Jun Hu, Mei-Fu Zhou, Julia M. Ribeiro, John Malpas, Ya-Dong Wu, Zhong-Jie Bai

© 2023. American Geophysical Union. All Rights Reserved.

Abstract To understand the oxygen fugacity (fO_2) during subduction initiation, we examined proto-arc boninites and associated mantle peridotites from the Troodos ophiolite, Cyprus. The Troodos ophiolite represents an exhumed piece of oceanic lithosphere that formed during subduction initiation in Neo-Tethys in Late Cretaceous. Dunites and surrounding harzburgites in the Kokkinorotsos podiform chromite deposit of the ophiolite were formed by reactions between peridotites and ascending boninitic magmas. The olivine-chromite oxybarometers show that the fO_2 values (ΔQFM -0.41 ± 0.37) of the dunites are slightly higher than those (ΔQFM -0.85 ± 0.52) of the harzburgites under mantle conditions, indicating that the mantle fO_2 was raised limitedly by percolation of the boninitic magmas. Meanwhile, the boninitic upper pillow lavas in the Margi area also recorded relatively reduced fO_2 values (ΔQFM -0.52 ± 0.20) during olivine-chromite crystallization, comparable to the fO_2 of mid-ocean ridge basalts. Shallow-level processes (i.e., magma ascent, crystallization, crustal assimilation, and degassing) appear to have limited influence on the estimated fO_2 values in Troodos. The similarly low fO_2 values of the mantle peridotites and boninitic magmas suggest that the Troodos primary boninitic magmas were perhaps not as oxidized as the Izu-Bonin-Mariana (IBM) proto-arc boninitic magmas, though both mantle sources have captured the slab fluids released during subduction inception. This difference might be attributed to the different nature of the slab components (i.e., a more reduced subduction input for Troodos). Our study thus suggests that subducted slabs might not always release oxidized fluids, and the oxidation processes might be different for each nascent subduction zones.

Plain Language Summary Subduction zones have played a key role in mass exchange between the Earth's surface and its interior, and are one of the main factories for the generation of Earth's magmas. The redox state of arc lavas produced at subduction zones controls the formation of important mineral deposits. In fact, subduction zone lavas are believed to be generally more oxidized than mid-ocean ridge lavas, but the origin of their oxidized nature and how their redox state change during the birth of a subduction zone remains poorly understood. Boninites are special Mg- and Si-rich but Ti-poor lavas ($SiO_2 > 52$ wt.%, $MgO > 8$ wt.%, and $TiO_2 < 0.5$ wt.%), and are typical products of magmatism that formed during subduction initiation. Here, we show that the primary boninitic magmas of the Troodos ophiolite of Cyprus are in fact no more oxidized than mid-ocean ridge basalts, even though their mantle source interacted with the slab fluids released from the incipient subducted plate. Therefore, we propose that proto-arc magmas, that formed as the down-going slab began foundering, might not always be oxidized during the inception of a subduction zone.

1. Introduction

Subduction zone lavas are believed to generally have high and variable oxygen fugacity (fO_2) values relative to mid-oceanic ridge basalts (MORBs) (e.g., Brounce et al., 2014; Christie et al., 1986; Cottrell et al., 2021; Evans et al., 2012; Kelley & Cottrell, 2009), yet the origin of such elevated fO_2 is widely debated (Kelley & Cottrell, 2009; Lee et al., 2005, 2010). The prevailing view is that high fO_2 values of arc lavas could be inherited from their mantle sources. In such a scenario, the sub-arc mantle was oxidized by the addition of slab-derived oxidized materials (e.g., ferric iron and sulfate) released during slab dehydration/melting (Ballhaus, 1993; Brounce et al., 2014; Kelley & Cottrell, 2009; Parkinson & Arculus, 1999; Wood et al., 1990). In contrast, the fact that primary arc magmas possess similar redox-sensitive ratios (V/Sc, Zn/Fe) and Cu contents to MORBs

suggests that primary arc magmas might have initial low fO_2 values similar to those of MORBs, and that their oxidation state was likely changed during crustal assimilation, magma fractionation, and magma degassing (Grocke et al., 2016; Lee et al., 2005, 2010, 2012; Moussallam et al., 2014, 2016; Tang et al., 2018).

Boninite is a type of subduction zone lava characterized by high MgO and SiO_2 contents and low TiO_2 contents (SiO_2 > 52 wt.%, MgO > 8 wt.%, and TiO_2 < 0.5 wt.%) (Crawford et al., 1989; Le Bas, 2000). Boninites are formed by re-melting of refractory mantle (i.e., that left after prior magma extraction) induced by the infiltration of slab-derived water-rich fluids and slab melts (e.g., Falloon & Danyushevsky, 2000; Pearce & Reagan, 2019; Pearce & Robinson, 2010; Reagan et al., 2010; Wood & Turner, 2009). The ramifications of their petrogenesis are two-fold: (a) the redox state of the refractory mantle source of boninites may be more easily controlled by the slab fluids than the pristine mantle (i.e., more fertile) source, because it may have lost large amounts of fO_2-buffered elements (e.g., iron and sulfur) (Cottrell & Kelley, 2011) through previous episodes of mantle melting; (b) melting of refractory mantle requires addition of larger amounts of slab-derived fluids/melts to lower its solidus (Falloon & Danyushevsky, 2000; Wood & Turner, 2009). The fO_2 values of the boninites may be used to elucidate whether this addition of slab-derived material has the potential to oxidize the proto-arc mantle, the source of subduction zone magmas. Here, the term "proto-arc" is used for the rocks that were erupted as the subducted plate began sinking. For instance, although the Izu-Bonin-Mariana (IBM) proto-arc crust is now emplaced in the modern fore-arc (Figure 1), here we will use the term "proto-arc" for these rocks.

Two proxies can be utilized to constrain the fO_2 of primary boninitic magmas, that is, erupted boninitic lavas and their associated peridotites. First, fO_2 of boninitic lavas can be directly measured using included olivine-chromite pairs (e.g., Evans et al., 2012) or glass shards (Brounce et al., 2015, 2021). However, shallow-level differentiation processes (e.g., magma degassing, fractionation, and crustal assimilation) may have modified the initial fO_2 of the primary boninitic magmas (Figure 1) (Brounce et al., 2015, 2021; Evans et al., 2012; Lee et al., 2005, 2010). Associated mantle peridotites in proto-arcs are thought to be genetically related to the boninitic magmas, either as the residue of mantle melting that produced these magmas, or as the melt-rock reaction products of the boninitic magmas passage through the upper mantle (e.g., Pearce et al., 2000; P. F. Zhang et al., 2020) (Figure 1). These proto-arc peridotites have not been affected by shallow-level differentiation processes, and can therefore serve as independent probes into the fO_2 of the primary boninitic magmas (Bénard et al., 2018; Birner et al., 2017, 2018).

The Troodos ophiolite of Cyprus is one of the most studied supra-subduction zone (SSZ) ophiolites in the world (e.g., Edwards et al., 2010; Miyashiro, 1973; Pearce & Robinson, 2010; Robertson & Xenophontos, 1993). It is characterized by two series of volcanic lavas, the tholeiitic lower pillow lavas (LPL) overlain by the boninitic upper pillow lavas (UPL), which have preserved relatively fresh glass shards (e.g., Pearce & Robinson, 2010; Robinson et al., 1983; Woelki et al., 2019, 2020), and has been proposed to develop during the earliest stages of development of a subduction zone (Figure 1) (Hu et al., 2021; Ishizuka et al., 2014; Pearce & Robinson, 2010). Therefore, it might provide new additional constraints to the processes that modulate the redox state of the magmas that formed during subduction inception. In this study, we examine the fO_2 of the primary boninitic magmas by investigating both the UPL and the associated metasomatized mantle peridotites of the Troodos ophiolite in Cyprus (Figure 2) (Hu et al., 2021; Ishizuka et al., 2014; Pearce & Robinson, 2010). The olivine-(orthopyroxene)-chromite oxybarometers of Davis et al. (2017) and Ballhaus et al. (1991) are used both for mantle peridotites and in boninites to infer the fO_2 of the primary boninitic magmas, because this can minimize potential effects of shallow-level igneous processes, for example, fractionation and degassing (e.g., Evans et al., 2012). Our new results, for both boninites and associated mantle peridotites, suggest that the fO_2 of primary boninitic magmas in the Troodos ophiolite was similar to that of MORBs, despite their interaction with the slab fluids (Pearce & Robinson, 2010), which reflects the release of relatively reduced slab fluids in the Troodos proto-arc mantle in Late Cretaceous time. Hence, we propose that subducted slab fluids may have oxidation states which vary from one subduction zone to another, and that the redox histories of magmas produced during subduction initiation are more complex than previously considered.

2. The Troodos Ophiolite

2.1. Geological Background

The island of Cyprus is made up of the Kyrenia terrane, the Mamonia Complex, and the Troodos ophiolite, which were assembled upon closure of the Neo-Tethys Ocean, and then covered by carbonate and siliciclastic sedimentary sequences (Figure 2a) (Edwards et al., 2010). The Troodos ophiolite contains two litho-stratigraphic

21699356, 2023, 4, Downloaded from https://agupubs.onlinelibrary.wiley.com/doi/10.1029/2022JB025008 by CAS - Chengdu Library, Wiley Online Library on [20/05/2024]. See the Terms and Conditions (https://onlinelibrary.wiley.com/terms-and-conditions) on Wiley Online Library for rules of use; OA articles are governed by the applicable Creative Commons License

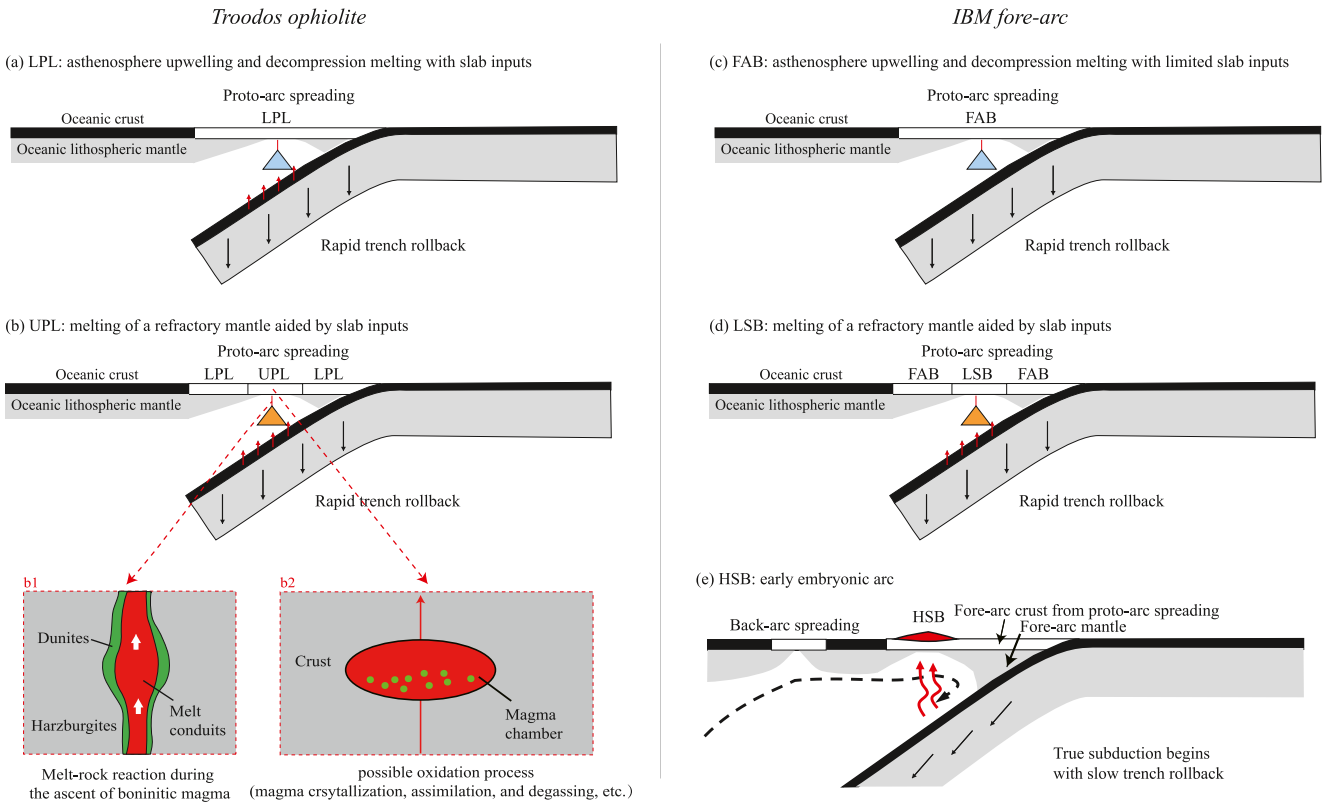

Figure 1. Schematic models of the formation of proto-arc lithospheres during the subduction initiation stage of the Troodos ophiolite (left) and the Izu–Bonin–Mariana (IBM) proto-arc (right), modified after Pearce and Robinson (2010), Stern et al. (2012) and Reagan et al. (2019). (a, b) Formation of the Troodos ophiolite: (a) as the subducted slab began to sink, the lower pillow lavas (LPL) were generated by melting of the ascending proto-arc asthenosphere infiltrated by slab fluids (Pearce & Robinson, 2010). Because boninites are derived from a more depleted mantle source than either the IBM fore-arc basalts (FABs) or the Troodos LPL, triangles with different colors are used to represent the melting region. (b) The upper pillow lavas are boninitic magmas that were generated by melting of a refractory mantle infiltrated by larger degrees of slab input relative to the LPL (Hu et al., 2021; Pearce & Robinson, 2010). (b1) Boninitic magmas ascended and reacted with the surrounding mantle peridotites to produce depleted harzburgites and dunites, and (b2) further experienced shallow-level differentiation processes before final eruption. (c–e) Formation of IBM proto-arc magmas: (c) FABs are the first magmas produced in IBM as the slab began sinking. FABs were generated by decompression melting of the proto-arc asthenosphere with limited slab input (Reagan et al., 2010, 2019; Shervais et al., 2019). (d) Low-silica boninites were then formed by melting of the residual proto-arc asthenosphere after FAB extraction, induced by fluids and melts released from the nascent subducted slab (Coulthard et al., 2021; Ishizuka et al., 2006, 2011; Reagan et al., 2010; Shervais et al., 2021). (e) After termination of rapid trench rollback and proto-arc spreading, high-silica boninites (HSB) began to form by melting of the residual and strongly depleted proto-asthenosphere that was assisted by the infiltration of slab fluids. HSB thus mark the onset of true arc magmatism in IBM (Coulthard et al., 2021; H. Y. Li et al., 2019; Reagan et al., 2010, 2017, 2019).

sequences, that is, the main Olympos (Axis) sequence and the Arakapas (Transform) sequence (Figure 2b) (Gass et al., 1994; Geological Survey Department Cyprus, 1995). The main Olympos (Axis) sequence is a complete ophiolite sequence that developed above an incipient subduction zone at ~92 Ma (Chen et al., 2020; Mukasa & Ludden, 1987). From bottom to top, it includes a serpentinized mantle unit, a plutonic unit, sheeted dykes, and both pillowed and massive lavas. This stratigraphic sequence was uplifted by serpentinite diapirism approximately 2 Ma ago (Schuiling, 2011). The Arakapas (Transform) sequence is bounded by a fossil transform fault to the north (Simonian & Gass, 1978) (Figure 2b), and although containing rock types generally similar to those of the main Olympos (Axis) Sequence, displays structural relationships disrupted by intensive deformation.

According to Batanova and Sobolev (2000), the mantle peridotites of the ophiolite can be divided into eastern (U1) and western (U2) parts (Figure 2c). U1 mainly consists of lherzolites containing low-Cr# ([atomic Cr/(Cr + Al) * 100 of chromites] = 22–28) chromite, and subordinate dunite bodies in association with clinopyroxene-bearing harzburgites (Batanova & Sobolev, 2000; Wilson, 1959). U1 peridotites are strongly serpentinized and show a variety of tectonic fabrics. U1 lherzolites have been interpreted as mantle residues, left after extraction of tholeiitic basalts, and subsequently modified by further melt percolation (Batanova & Sobolev, 2000). In comparison, U2 peridotites are less serpentinized, and comprise refractory harzburgites and dunites associated with podiform chromite deposits. U2 harzburgites have high Cr# (51–70) chromites and a very

21699356, 2023, 4, Downloaded from https://agupubs.onlinelibrary.wiley.com/doi/10.1029/2022JB025008 by CAS - Chengdu Library, Wiley Online Library on [20/05/2024]. See the Terms and Conditions (https://onlinelibrary.wiley.com/terms-and-conditions) on Wiley Online Library for rules of use; OA articles are governed by the applicable Creative Commons License

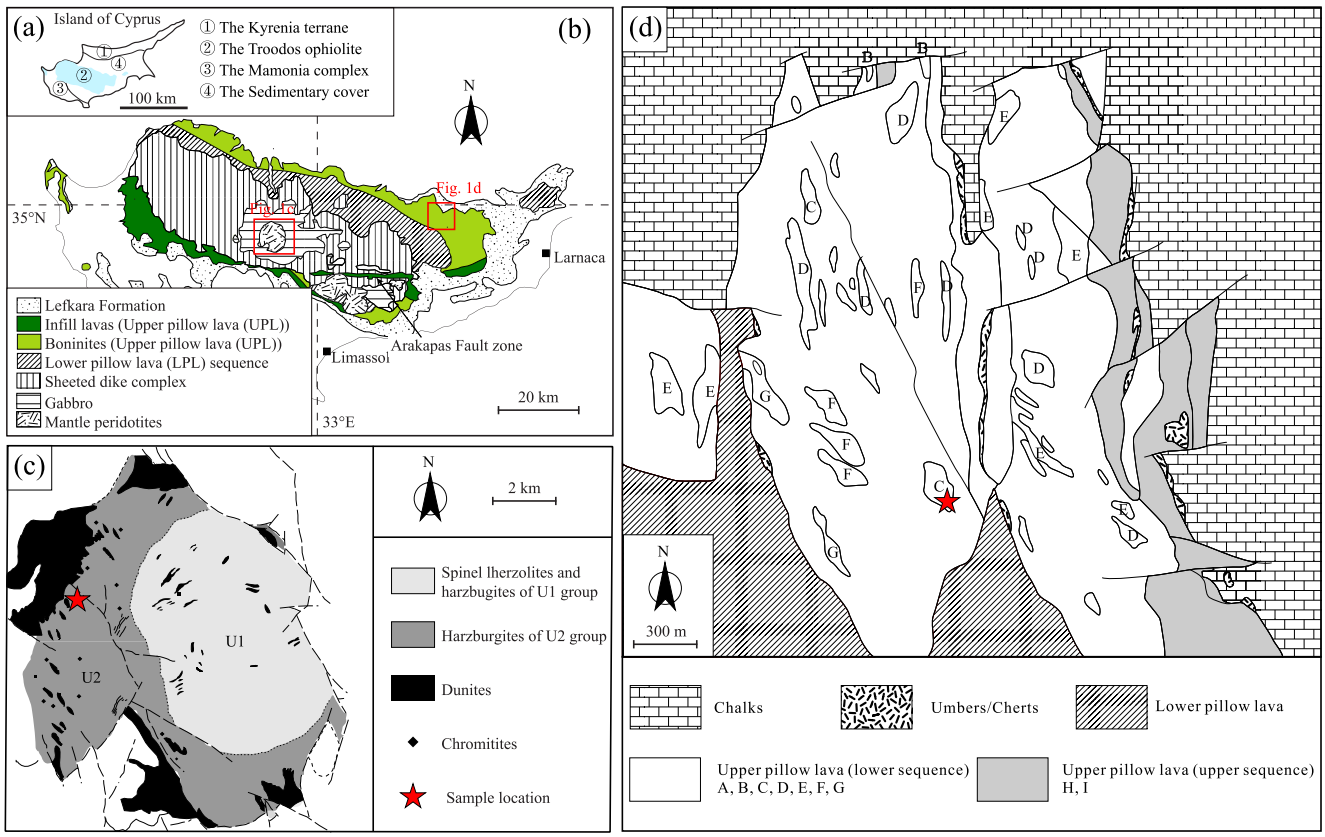

Figure 2. Simplified map of (a) the island of Cyprus and (b) the Troodos ophiolite, modified after Osozawa et al. (2012) and Regelous et al. (2014). (c) Geological map of the Margi area, modified after Bailey et al. (1991). The lower part of the upper pillow lava suite (upper pillow lavas (UPL)) includes: A— "crystalline" olivine-phyric pillows and thin flows; B— "glassy" olivine-phyric pillows; C—picritic pillows; D—massive picritic flows; E—aphyric massive flows; F—olivine microphyric flows; G—clinopyroxene microphyric flows. The upper part of the UPL includes: H—aphyric pillows and thin flows; I—olivine-phyric pillows and flows. (d) Geological map of the mantle peridotites in the Troodos ophiolite after Batanova and Sobolev (2000).

small modal percentage of clinopyroxene (<1%) (Batanova & Sobolev, 2000). They show northwest-trending tectonite fabrics and evidence of high-temperature deformation together with the overlying dunites and cumulates (George, 1978; Malpas, 1990). Most podiform chromite deposits of the Troodos ophiolite are hosted by the U2 peridotites, and orebodies are generally enveloped by dunites (Greenbaum, 1977). U2 harzburgites, dunites, and podiform chromitites have been interpreted as products of reaction between infiltrating melts (most likely boninitic magmas) and lherzolites (Batanova & Sobolev, 2000; Büchl et al., 2002, 2004).

Volcanic rocks of the Troodos ophiolite comprise two sequences, that is, the LPL and the upper pillow lavas (UPL) (Figure 2a). The LPL are represented by tholeiitic basalts to basaltic andesites (Figure 3a), and are divided into Unit I rocks that are mafic-ultramafic in composition, overlying Unit II rocks that are intermediate-silicic in composition, followed by Unit III rocks that are mafic to mafic-intermediate in composition (Pearce & Robinson, 2010). Below the LPL is the Basal Group consisting of lavas and dykes that pass downwards into sheeted dykes (Geological Survey Department Cyprus, 1995; Pearce & Robinson, 2010). The UPL contains two groups of boninites. The first, which is mainly distributed on the northern side of the main Troodos sequence (Figure 2b), is locally separated from the LPL by discontinuous, thin sedimentary layers (Bailey et al., 1991). The second occurs in the south (Figure 2b), and it is associated with volcanic breccias that mark a fossil transform fault zone (Osozawa et al., 2012). These form the stratigraphically highest lavas, and were named "infill lavas" by Gass et al. (1994). The two groups of boninites are generally overlain by umberiferous sediments of the Perapedhi Formation (late Campanian; ca. 75 Ma), but interestingly, there are reports of some boninites of second group affinity, with Ar-Ar age of 55.5 ± 0.9 Ma, covered by middle sedimentary rocks of Paleogene to early Miocene age (Osozawa et al., 2012), and the relationship between the infill boninitic lavas and the main Olympos (Axis) Sequence remains enigmatic at present. For instance, regarding its tectonic setting, the second group of boninites has been proposed to be generated only in the proto-arc mantle beneath the Arakapas Fault Zone (Murton, 1989;

21699356, 2023, 4, Downloaded from https://agupubs.onlinelibrary.wiley.com/doi/10.1029/2022JB025008 by CAS - Chengdu Library, Wiley Online Library on [20/05/2024]. See the Terms and Conditions (https://onlinelibrary.wiley.com/terms-and-conditions) on Wiley Online Library for rules of use; OA articles are governed by the applicable Creative Commons License

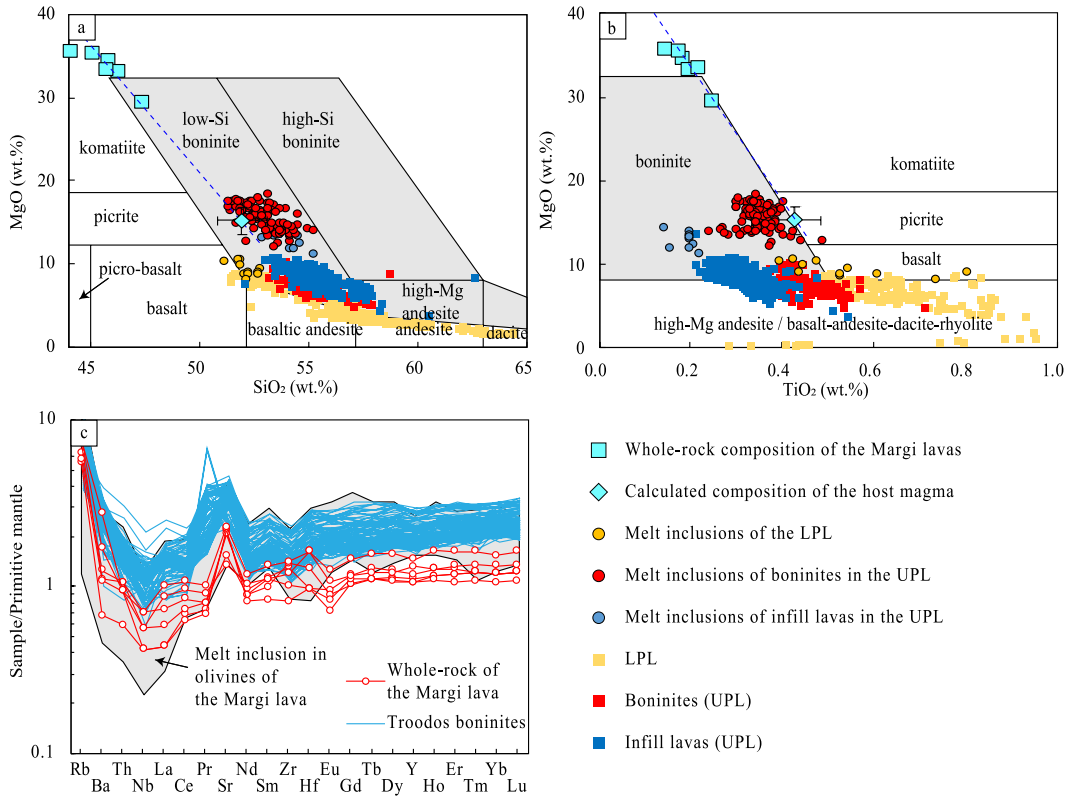

Figure 3. (a–b) Major element compositions of the Margi lavas of the Troodos ophiolite. Compositions of host magmas of the olivine phenocrysts, that is, from the groundmass of the Margi lavas, are calculated by linear regression between MgO and other elements using ISOPLOT (Ludwig, 2003). The classification diagrams in (a) and (b) are from Pearce and Reagan (2019). (c) Primitive mantle-normalized trace element patterns of whole rocks of the Margi pillow lavas, in comparison with the melt inclusions hosted by olivine phenocrysts and the Troodos boninites. The normalization values are from Sun and McDonough (1989). Data source for the Troodos ophiolite: the melt inclusions of the LPL (Portnyagin et al., 1997); the melt inclusions of the boninites in the UPL (Hu et al., 2021); the melt inclusions of the infill lavas in the UPL (Portnyagin et al., 1996); volcanic glasses of LPL and UPL are from Pearce and Robinson (2010), Osozawa et al. (2012), Regelous et al. (2014), Golowin et al. (2017), Woelki et al. (2018, 2019, 2020). Further classification of LPL and UPL of the Troodos ophiolite are after Pearce and Robinson (2010) and Osozawa et al. (2012), respectively. LPL—lower pillow lava; UPL—upper pillow lava. Note that the Troodos boninites are all LSB.

Rogers et al., 1989). For brevity, in this study we follow the names used by Gass et al. (1994) and Osozawa et al. (2012), the first group being "the boninites" and the second group being "the infill lavas."

The chemostratigraphy of lavas of the Troodos ophiolite is similar to that observed in the Izu–Bonin–Mariana (IBM) proto-arc system (Hu et al., 2021; Ishizuka et al., 2014; Pearce & Robinson, 2010). As such, along with paleogeographic reconstructions (Pearce & Robinson, 2010; X. Zhou et al., 2018), the Troodos ophiolite is considered to have developed during the early stages of an intra-oceanic subduction zone (Hu et al., 2021; Ishizuka et al., 2014; Pearce & Robinson, 2010). However, the Troodos ophiolite lacks arc volcanic edifices, well developed volcanogenic sediments and thick felsic/andesitic crust, meaning there is no typical arc magmatism in the Troodos subduction zone (Osozawa et al., 2012; Pearce & Robinson, 2010). In the classification diagram of Pearce and Reagan (2019), the Troodos boninitic lavas are low-silica boninites (LSB); and high silica boninites (HSB) like those that marked the onset of arc magmatism in IBM (Reagan et al., 2010, 2019), have not been observed (Figures 3a and 3b). All this suggests that magmatism in the Troodos ophiolite developed before the onset of any true arc magmatism (Pearce & Robinson, 2010), and that Troodos subduction was not long-lived.

2.2. Samples and Petrography

This study focuses on boninites and mantle peridotites in the main Olympos (Axis) sequence of Troodos (Figure 2).

21699356, 2023, 4, Downloaded from https://agupubs.onlinelibrary.wiley.com/doi/10.1029/2022JB025008 by CAS - Chengdu Library, Wiley Online Library on [20/05/2024]. See the Terms and Conditions (https://onlinelibrary.wiley.com/terms-and-conditions) on Wiley Online Library for rules of use; OA articles are governed by the applicable Creative Commons License

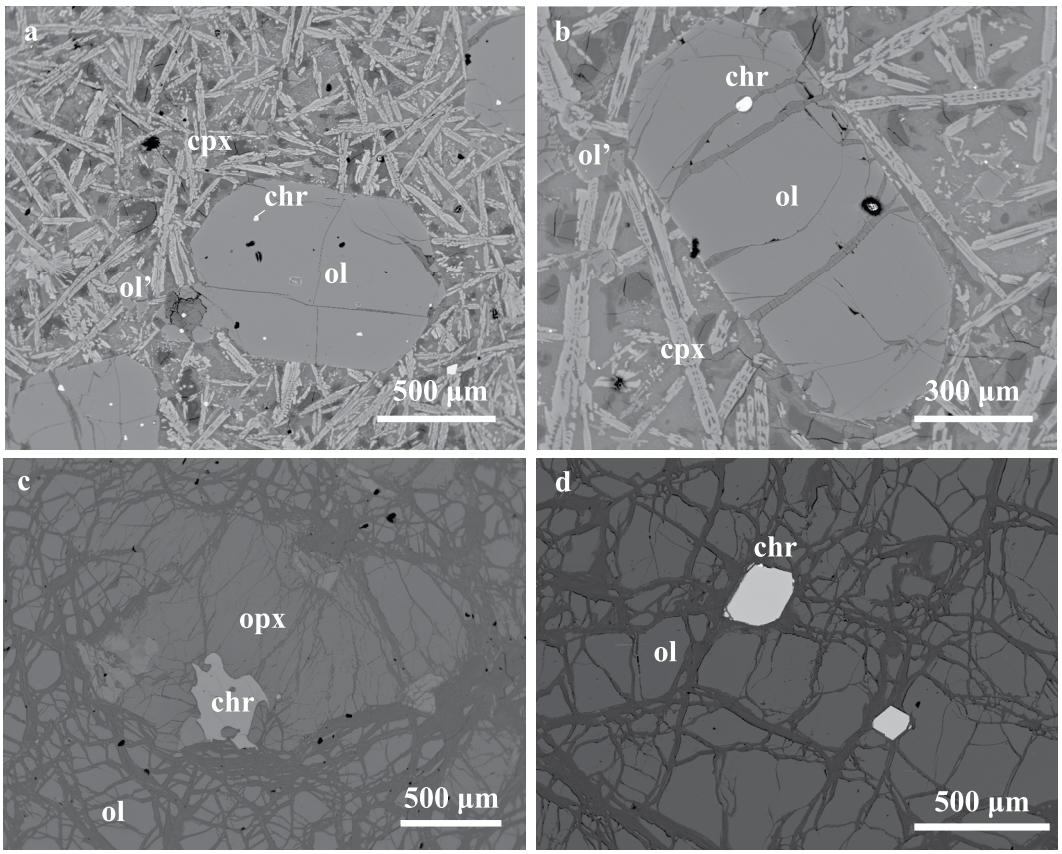

Figure 4. Backscattered electron images of the pillow lavas and the mantle peridotites of the Troodos ophiolite. (a–b) Pillow lavas show typical vitrophyric texture, with large and euhedral olivine phenocrysts in a glassy groundmass; (c) harzburgites; (d) dunites. Ol—olivine; Opx—orthopyroxene; Cpx—clinopyroxene; Chr—chromite. Ol' represents small olivine grains in the groundmass of the Margi lava.

The Margi area on Mt Olympos' northern flank is a classic locality for boninites in the ophiolite (Bailey et al., 1991; Gass, 1958; Malpas & Langdon, 1984; Sobolev et al., 1991) (Figure 2d). The LPL in Margi comprise aphyric to plagioclase and clinopyroxene micro-phyric volcanic rocks, and are separated from the UPL by a discontinuous thin sedimentary layer (Bailey et al., 1991). The UPL in this locality have been divided into two petrographic sequences, a lower sequence of mainly olivine-phyric lavas and an upper sequence of essentially aphyric lavas (Figure 2d) (Bailey et al., 1991). Such stratification may reflect settling of olivine crystals in the magma supply system. Olivine-rich pillow lavas in the lower sequence show typical vitrophyric texture, with large and euhedral olivine phenocrysts set in a glassy groundmass composed of skeletal/dendritic crystals of clinopyroxene and small euhedral crystals of olivine and chromite (Figures 4a and 4b).

Harzburgites and dunites of the podiform chromite deposit in the Kokkinorotsos area of the U2 peridotites were sampled in this study (Figure 2c). Previous studies have shown that these peridotites were formed by progressive interaction between harzburgites and percolating boninitic magmas during the formation of the chromite deposit (Figures 1b1 and 1b2) (Büchl et al., 2004). The harzburgites are porphyroclastic and coarse-grained, and consist of olivine, orthopyroxene, clinopyroxene and chromite (Figure 4c). Orthopyroxene and olivine occur as large porphyroclasts, whereas clinopyroxene mainly occurs as small recrystallized grains within or around these phases. Chromite in the harzburgites has a variety of shapes from anhedral to euhedral. Dunites are mainly composed of olivine and chromite (Figure 4d), and most chromite grains are euhedral. In some places they display pull-apart textures and are aligned with the mantle tectonite fabric.

21699356, 2023, 4, Downloaded from https://agupubs.onlinelibrary.wiley.com/doi/10.1029/2022JB025008 by CAS - Chengdu Library, Wiley Online Library on [20/05/2024]. See the Terms and Conditions (https://onlinelibrary.wiley.com/terms-and-conditions) on Wiley Online Library for rules of use; OA articles are governed by the applicable Creative Commons License

3. Analytical Methods

Whole-rock major and trace elements of lavas were determined in the Australian Laboratory Services (ALS) P/L using X-ray fluorescence (XRF) and inductively coupled plasma mass spectrometry (ICP-MS), respectively. The relative standard deviations (RSDs) for both major and trace elements are better than 5%.

Element compositions of minerals were measured by a JEOL JXA-8230 electron probe micro-analyzer (EPMA) at the Department of Earth Sciences, the University of Hong Kong (DES, HKU). Accelerating voltage and probe current were 20 kV and ~20 nA. The beam diameter was 1 μm. The peak counting time was 10–20 s for major elements and 120 and 40 s, respectively, for Ti and V of chromites. Olivine and chromite in-house standards were used to monitor the data quality. For major elements, for example, Al_2O_3, Cr_2O_3, MgO, and FeO of chromite, and MgO, FeO, and SiO_2 of olivine, the measured results were in accordance with the referenced values within ±3%. For trace elements with concentrations close to 0.1–0.3 wt.%, for example, TiO_2, V_2O_3, MnO, ZnO, and NiO of chromite, and NiO of olivine, the measured results were in accordance with the referenced values within 5%–20% (Table S1 in Supporting Information S2).

The $Fe^{3+}/\Sigma Fe$ of chromite is crucial for calculation of oxygen fugacity, and therefore it must be determined accurately. This study adopted secondary chromite standards with $Fe^{3+}/\Sigma Fe$ certified by Mössbauer spectroscopy to correct the $Fe^{3+}/\Sigma Fe$ data from EPMA (Wood & Virgo, 1989). The difference between $Fe^{3+}/\Sigma Fe$ measured by Mössbauer ($(Fe^{3+}/\Sigma Fe)_{Möss}$) and $Fe^{3+}/\Sigma Fe$ calculated by stoichiometry ($(Fe^{3+}/\Sigma Fe)_{Stoichiometry}$) using EMPA data, is linearly related to the Cr# of the chromite:

$$\left(Fe^{3+}/\Sigma Fe\right)_{Möss} - \left(Fe^{3+}/\Sigma Fe\right)_{Stoichiometry} = A + B * (Cr\#) \quad (1)$$

where A and B are constants. This study used secondary chromite standards from Dare et al. (2009) (DB8803.3, KLB8316, VI314.5, MBR8306, and HR04-18) to build the calibration line (Table S2 in Supporting Information S2).

Trace elements of chromite of peridotites were analyzed using the 193 nm wavelength excimer GeolasPro laser ablation system coupled to an Agilent 7700e ICP-MS, at the Wuhan Sample Solution Analytical Technology Co., Ltd., Wuhan, China. The spot size and frequency of the laser were set to 44 μm and 6 Hz, respectively. Multiple US Geological Survey reference materials (BHVO-2G, BCR-2G, and BIR-1G) were used as calibration standards with Al as the internal standard. NIST610 was measured for quality control of the time-dependent calibration for sensitivity drift. The trace element data were treated offline using the ICPMSDataCal software (Liu et al., 2008). Calibration curves yield $r^2 \geq 0.999$ relative to the reported standard values for elements of interest in this study. Precision (1RSD) was estimated by repeat analysis of the standards, which was generally better than 10% for elements of interest (Table S3 in Supporting Information S2). Reproducibility of replicate analyses of examined chromite grains are ≤15% RSD for Ga, ≤10% RSD for other interested elements (Sc, Ti, V, Mn, Co, Ni, and Zn) (Table S4 in Supporting Information S2). The Ti concentrations of chromite measured by LA-ICP-MS are consistent with data measured by EPMA, confirming the validity of the laser data (Figure S1 in Supporting Information S1).

Trace element concentrations of chromite inclusions in olivine phenocrysts of the lavas were analyzed at the State Key Laboratory of Nuclear Resources and Environment (SKLNRE), East China University of Technology. The analytical instruments consist of a PerkinElmer NexION 1000 ICP-MS coupled to an ESL NWR-193 laser ablation system. The spot size and frequency of the laser were set to 30 μm and 5 Hz to avoid contamination of host olivines. Element abundances were also calibrated using the ICPMSDataCal software. NIST610 and NIST612 were used as the external standard and Al contents were selected as the internal standard. Calibration curves yield $r^2 \geq 0.999$ relative to the reported standard values for elements of interest in this study. Analytical accuracy, as estimated by repeated analyses of the NIST 614 standard, was in accordance with the reference values within ±15% for elements of interest except Sc (average Sc value = 1.35 ppm, reference Sc value = 0.74 ppm) (Table S3 in Supporting Information S2). This discrepancy can be explained by the interference of $^{29}Si^{16}O$ on ^{45}Sc. For NIST614 glass containing 72.1 wt.% SiO_2 and 0.74 ppm Sc, $^{29}Si^{16}O$ produces a significant inference on ^{45}Sc of about 0.6 ppm Sc. However, this interference effect is negligible because the primary standards (NIST610 and NIST612) have very high Sc contents (455 and 39.9 ppm, respectively), and the chromites have very low SiO_2 contents (<0.1 wt.%).

21699356, 2023, 4, Downloaded from https://agupubs.onlinelibrary.wiley.com/doi/10.1029/2022JB025008 by CAS - Chengdu Library, Wiley Online Library on [20/05/2024]. See the Terms and Conditions (https://onlinelibrary.wiley.com/terms-and-conditions) on Wiley Online Library for rules of use; OA articles are governed by the applicable Creative Commons License

Table 1
Summary of Mineral Compositions of Mantle Peridotites From the Troodos Ophiolite, Cyprus

Sample	Olivine Fo	Orthopyroxene Mg#	Orthopyroxene $X_{M1}^{Fe} * X_{M2}^{Fe}$	Chromite Cr#	Chromite Mg#	Chromite TiO_2 (wt.%)	Chromite $Fe^{3+}/\sum Fe$	Chromite aFe_3O_4
Harzburgite								
CY-H5	91.5	91.6	0.0064	72.7	47.1	0.05	0.13	0.006
CY-H6	91.3	91.5	0.0065	69.5	49.6	0.02	0.12	0.005
CY-H7	91.1	91.5	0.0066	67.1	51.8	0.02	0.08	0.002
CY-H8	91.2	91.6	0.0064	70.4	47.9	0.01	0.14	0.007
CY-H9	91.1	91.3	0.0067	60.2	53.2	0.01	0.08	0.003
CY-H10	91.2	91.4	0.0069	72.1	45.9	0.01	0.13	0.007
CY-H11	91.2	91.6	0.0064	70.4	48.2	0.02	0.12	0.006
Dunite								
CY-D3	91.8	–	–	77.7	45.6	0.13	0.14	0.007
CY-D5	91.9	–	–	76.7	46.4	0.14	0.14	0.007
CY-D6	91.8	–	–	72.7	50.0	0.15	0.12	0.005
CY-D7	91.7	–	–	77.0	47.0	0.12	0.15	0.007
CY-D8	92.1	–	–	75.9	49.2	0.14	0.14	0.006
CY-D9	90.3	–	–	79.9	39.7	0.10	0.18	0.015
CY-D10	90.3	–	–	76.8	41.0	0.13	0.15	0.011
CY-D11	92.0	–	–	72.0	49.7	0.07	0.19	0.014
CY-D13	92.1	–	–	72.7	50.5	0.07	0.22	0.018
CY-D14	92.4	–	–	66.3	53.3	0.13	0.18	0.014
CY-D16	91.9	–	–	67.5	52.9	0.11	0.18	0.012

Element mapping of representative olivine and chromite grains was carried out using a JEOL JXA-8230 EPMA at DES, HKU. Operating conditions were as follows: accelerating voltage 15 kV; beam current 20 nA; probe diameter 1 μm dwell at 100 ms. The spatial distributions of Mg, Fe, Cr, and Al were determined.

The oxygen isotope compositions of olivine grains in the lavas were measured in situ using a CAMECA IMS-1280 Secondary Ion Microprobe Spectrometer (SIMS) at the Institute of Geology and Geophysics, Chinese Academy of Sciences (IGGCAS). The Cs^+ primary beam of ~2 nA accelerated to 10 kV was rastered over a 10 × 20 μm^2 area. In order to compensate for sample charging, an electron gun was used. Oxygen isotopes (^{18}O, ^{16}O) were measured statically in multi-collector mode with two off-axis Faraday cups, following the procedures given in X. H. Li et al. (2010). All measured $^{18}O/^{16}O$ values were normalized to those of Vienna Standard Mean Ocean Water (VSMOW; $(^{18}O/^{16}O)_{V-SMOW} = 0.0020052$). The standard San Carlos olivine ($\delta^{18}O = 5.2‰$, Eiler et al., 1995) was used as the external standard to correct the instrumental mass fractionation. The long-term precision of the measurements, as monitored by the Scan Carlos olivine, is 0.4‰.

4. Results

4.1. Mantle Peridotites

Representative mineral compositions of both harzburgites and dunites are listed in Table 1, and a full data set is available in the supplementary file (Table S5 in Supporting Information S2). Minerals in harzburgites and dunites have homogenous compositions with no compositional zoning, indicating that the composition of minerals may have reached equilibrium (Figures 5a–5c). Major element compositions of olivine and chromite are within the range of those of fore-arc peridotites (Arai, 1994; Pearce et al., 2000) (Figure S2 in Supporting Information S1). In the harzburgites, olivine has high Fo (atomic $Mg/(Mg + Fe^{2+}) \times 100$) ranging from 91.1 to 91.5, and chromite has high Cr# (60.2–72.7) and Mg# (atomic $Mg/(Mg + Fe^{2+}) \times 100$) (45.9–53.2) (Figure 6a). In addition, chromite in harzburgites has low TiO_2 (<0.06 wt.%) similar to that of fore-arc peridotites (Parkinson

21699356, 2023, 4, Downloaded from https://agupubs.onlinelibrary.wiley.com/doi/10.1029/2022JB025008 by CAS - Chengdu Library, Wiley Online Library on [20/05/2024]. See the Terms and Conditions (https://onlinelibrary.wiley.com/terms-and-conditions) on Wiley Online Library for rules of use; OA articles are governed by the applicable Creative Commons License

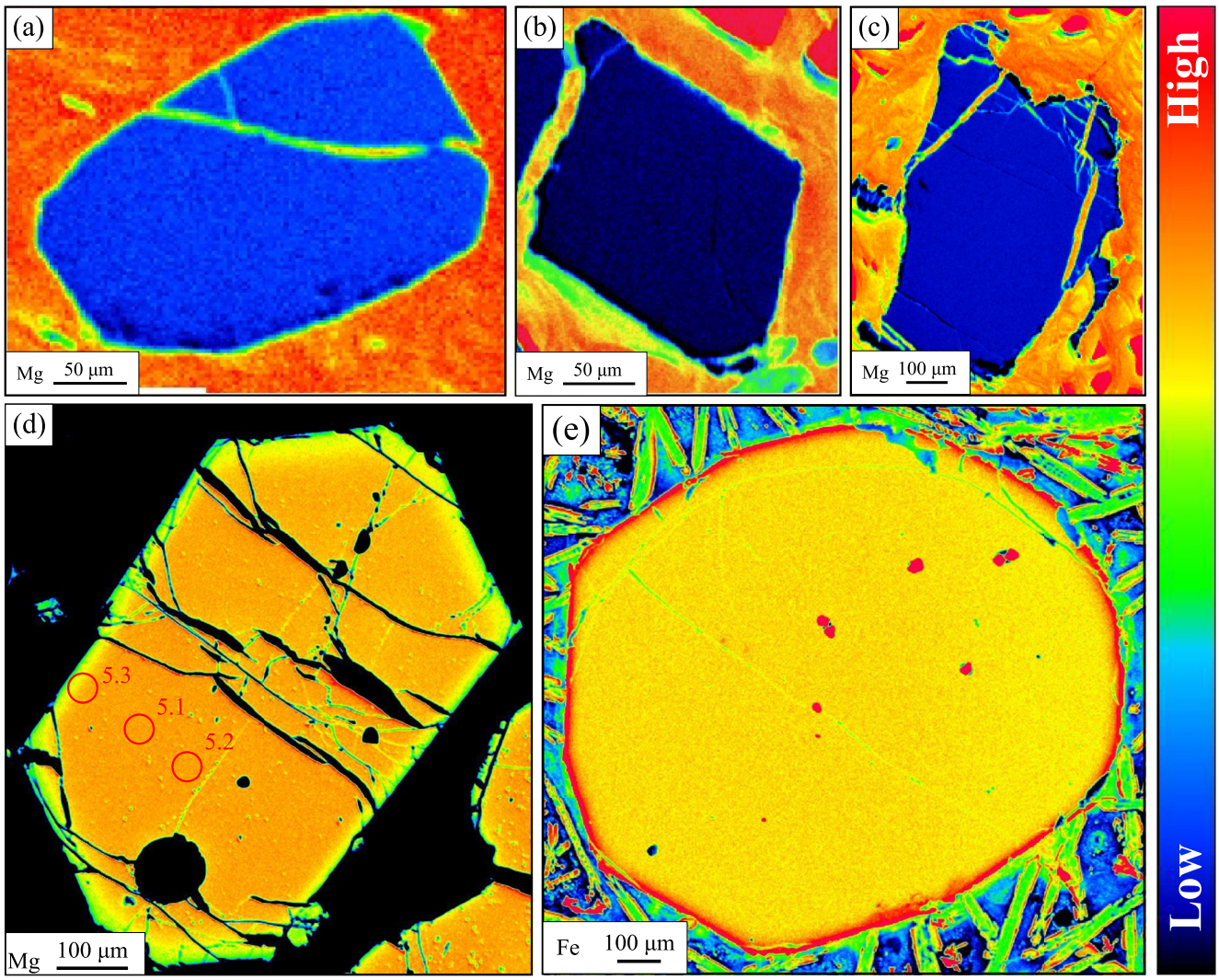

Figure 5. Element mapping of minerals in the mantle peridotites and the Margi lavas of the Troodos ophiolite. (a) Mg mapping of a chromite grain in a harzburgite; (b–c) Mg mapping of chromite grains in dunites; (d) Mg mapping of olivine phenocrysts in pillow lavas. Red circle and number represent the analysis position and values of $\delta^{18}O$, respectively. (e) Fe mapping of olivine phenocrysts in pillow lavas. The narrow rim of the olivine phenocryst indicates rapid cooling of the lavas.

& Pearce, 1998; Pearce et al., 2000) (Figure 6b), and $Fe^{3+}/\Sigma Fe$ from 0.08 to 0.14. Coexisting orthopyroxene has high Mg#, ranging from 91.3 to 91.6. In comparison, dunites contain olivine with higher Fo (90.3–92.4), and chromite with higher Cr# (66.3–79.9), TiO_2 (0.07–0.15 wt.%) and $Fe^{3+}/\Sigma Fe$ (0.12–0.22) than chromite in the harzburgites (Figure 6 and Table 1). Trace element compositions of chromite are listed in Table S6 in Supporting Information S2. Titanium shows different linear correlations with Sc and V (Figures 6c and 6d). Spinel in dunites has higher Sc (5.07–10.55 ppm) and lower V (1,015–1,428 ppm) than spinel in harzburgites (Sc: 2.72–5.22 ppm; V: 1,650–2,038 ppm).

4.2. Lavas

Whole-rock major and trace element compositions of the Margi lavas are provided in Table 3. Due to the large abundances of olivine phenocrysts, the Margi lavas are highly enriched in MgO, ranging from 28.4 wt.% to 34.2 wt.% (Figure 3). MgO exhibits clear relationships with other major elements, indicating that the whole rock compositions of the lavas are controlled by accumulation of olivine crystals (Figures 3a and 3b). For instance, with the increase of MgO from 28.4 wt.% to 34.2 wt.%, SiO_2 and TiO_2 decrease from 45.6 wt.% to 41.5 wt.% and from 0.24 wt.% to 0.14 wt.%, respectively. In the primitive mantle–normalized spider diagrams, whole-rock compositions of the Margi lavas show depletion in high field strength elements (HFSE) (e.g., Nb, Hf, Zr) and

21699356, 2023, 4, Downloaded from https://agupubs.onlinelibrary.wiley.com/doi/10.1029/2022JB025008 by CAS - Chengdu Library, Wiley Online Library on [20/05/2024]. See the Terms and Conditions (https://onlinelibrary.wiley.com/terms-and-conditions) on Wiley Online Library for rules of use; OA articles are governed by the applicable Creative Commons License

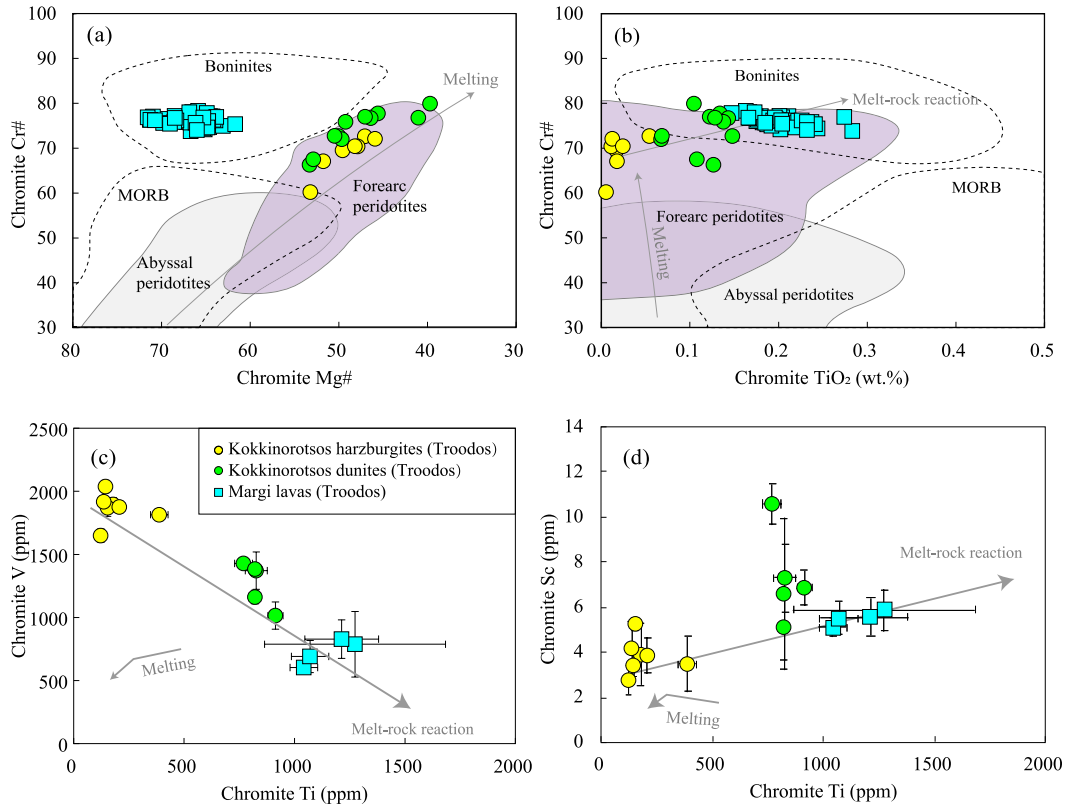

Figure 6. (a, b) Major element compositions of chromites in the Kokkinorotsos mantle peridotites and the Margi lavas of the Troodos ophiolite. (c, d) Ti-Sc and Ti-V systematics in chromites, indicate that melt-rock reaction controls the composition of chromites. The trend in mantle melting was simulated using a batch model of depleted mantle from Workman and Hart (2005), with distribution coefficients from Le Roux et al. (2015), and melting equation (0.571 Opx + 0.735 Cpx + 0.041 Chr = 0.347 Ol + 1 liquid; 1.25 Opx = 0.25 Ol + 1 liquid) from Wasylenki et al. (2003) and Parman and Grove (2004). Data source: mid-oceanic ridge basalt and boninite (Barnes & Roeder, 2001), abyssal peridotites (Warren, 2016 and references therein), and forearc peridotites (Parkinson & Pearce, 1998; Pearce et al., 2000).

variable enrichment in fluid-mobile elements (e.g., Ba, Cs, Sr, and Rb, Pb) (Figure 3c), similar to the compositions of boninitic lavas in the Troodos ophiolite and the melt inclusions hosted in the olivine phenocrysts of the Margi lavas (Hu et al., 2021). The absolute concentrations of incompatible trace elements are lower than those of olivine-hosted melt inclusions due to the buffering effects of olivine, but the ratios between trace elements that are strongly incompatible to olivine are not affected by this effect. For instance, whole rock Sr/Zr and Ba/Nb range from 2.1 to 5.1 and 15 to 39, respectively, which is within the compositional range of the olivine-hosted melt inclusions (Sr/Zr: 2.6–4.4; Ba/Nb: 13–40) (Hu et al., 2021).

Representative major element compositions of olivine and chromite from lavas in the Margi area are listed in Table 2, with the complete data set in the supplementary file (Table S7 in Supporting Information S2). The olivine phenocrysts have narrow rims with uniform core compositions, indicating rapid cooling after eruption (Figures 5d and 5e). The olivine phenocrysts are Mg-rich forsterite (MgO: 47.3–52.7 wt.%; Fo: 90.5–93.2), and they possess chromite inclusions with high Cr# ranging from 73.8 to 78.3 and TiO_2 ranging from 0.15 wt.% to 0.28 wt.%, which are within the range of chromites hosted in the boninites (Figure 6). $Fe^{3+}/\Sigma Fe$ of these olivine-hosted chromite inclusions range from 0.20 to 0.29. Trace element concentrations of the olivine-hosted chromite inclusions are listed in Table S6 in Supporting Information S2. They have high Sc (5.06–5.82 ppm) and low V (603–828 ppm), which plot along the trend defined by chromites from harzburgites and dunites (Figures 6c and 6d).

Oxygen isotope compositions of olivines are provided in the supplementary file (Table S8 in Supporting Information S2). Olivine phenocrysts have mantle-like $\delta^{18}O$ (5.2 ± 0.6; 2σ, n = 66) (Figure 7). Within a single grain, oxygen isotopes are relatively constant within the error range of measurement, despite distance to the crystal

21699356, 2023, 4, Downloaded from https://agupubs.onlinelibrary.wiley.com/doi/10.1029/2022JB025008 by CAS - Chengdu Library, Wiley Online Library on [20/05/2024]. See the Terms and Conditions (https://onlinelibrary.wiley.com/terms-and-conditions) on Wiley Online Library for rules of use; OA articles are governed by the applicable Creative Commons License

Table 2
Summary of Olivine-Chromite Pairs in the Margi Lavas of the Troodos Ophiolite for the Olivine-Chromite Oxybarometer

No. of olivine-chromite pairs	OlivineFo	ChromiteCr#	ChromiteMg#	Chromite TiO_2 (wt.%)	Chromite $Fe^{3+}/\sum Fe$	$T_{ol\text{-}chr}$ (℃)[a]	log fO_2 (ΔQFM)[b]	log fO_2 (ΔQFM)[c]
CYMB1702-01	91.4	78.0	66.5	0.17	0.23	1207	0.39	-0.52
CYMB1702-03	90.8	77.1	64.5	0.18	0.23	1190	0.43	-0.44
CYMB1702-04	91.4	75.7	64.6	0.18	0.21	1146	0.33	-0.65
CYMB1702-05	93.0	76.5	70.0	0.20	0.22	1159	0.47	-0.67
CYMB1702-06	91.5	78.3	65.9	0.16	0.21	1184	0.26	-0.68
CYMB1702-07	93.0	76.3	71.3	0.19	0.24	1193	0.51	-0.59
CYMB1702-08	93.2	77.1	71.0	0.17	0.22	1174	0.43	-0.71
CYMB1702-09	90.9	77.1	64.2	0.21	0.21	1176	0.17	-0.72
CYMB1702-10	93.2	76.9	71.6	0.20	0.22	1185	0.36	-0.77
CYMB1704-01	91.2	77.8	64.9	0.15	0.21	1179	0.27	-0.64
CYMB1704-02	91.9	75.8	67.1	0.24	0.20	1165	0.15	-0.86
CYMB1704-03	90.9	74.7	64.6	0.23	0.24	1176	0.48	-0.40
CYMB1704-04	90.9	73.8	66.7	0.28	0.29	1216	0.80	-0.05
CYMB1704-05	91.7	77.2	68.5	0.20	0.24	1223	0.39	-0.54
CYMB1704-06	91.0	75.3	65.2	0.19	0.21	1177	0.23	-0.67
CYMB1704-07	90.9	76.0	66.7	0.18	0.28	1234	0.65	-0.17
CYMB1704-08	91.3	76.2	67.5	0.21	0.21	1219	0.10	-0.79
CYMB1705-01	92.5	75.6	69.8	0.21	0.24	1185	0.53	-0.53
CYMB1705-02	90.9	74.2	65.1	0.20	0.25	1181	0.52	-0.36
CYMB1705-03	92.9	76.3	71.2	0.18	0.22	1191	0.29	-0.81
CYMB1705-04	91.8	75.7	66.7	0.21	0.23	1167	0.49	-0.50
CYMB1707-01	91.1	76.2	64.9	0.19	0.25	1181	0.63	-0.27
CYMB1707-02	91.1	75.0	63.1	0.19	0.24	1133	0.62	-0.33
CYMB1707-03	90.7	76.8	64.3	0.19	0.24	1194	0.50	-0.34
CYMB1707-04	91.3	76.4	65.3	0.20	0.22	1172	0.37	-0.57
CYMB1707-05	90.8	76.2	63.9	0.19	0.24	1176	0.48	-0.39
CYMB1707-06	91.2	76.7	64.7	0.17	0.22	1168	0.40	-0.53
CYMB1707-07	90.5	76.3	64.1	0.20	0.24	1196	0.43	-0.39
CYMB1708-01	91.2	76.1	65.1	0.20	0.20	1168	0.12	-0.81
CYMB1708-02	91.1	77.0	63.8	0.27	0.23	1158	0.47	-0.46
CYMB1708-03	91.2	74.4	65.2	0.24	0.25	1165	0.60	-0.33
CYMB1708-04	90.9	76.1	64.7	0.22	0.25	1182	0.56	-0.33
CYMB1709-02	90.9	74.6	64.8	0.22	0.25	1180	0.57	-0.31
CYMB1709-03	91.9	78.0	66.9	0.17	0.21	1180	0.25	-0.74
CYMB1710-01	92.3	76.2	68.3	0.23	0.23	1169	0.53	-0.52
CYMB1710-02	91.1	76.8	65.3	0.20	0.21	1185	0.22	-0.68
CYMB1710-03	91.3	75.7	66.2	0.19	0.24	1184	0.47	-0.45
CYMB1713-01	90.8	75.3	61.7	0.24	0.22	1123	0.48	-0.45
CYMB1714-01	92.6	76.2	70.7	0.20	0.24	1203	0.50	-0.55
CYMB1714-02	92.0	75.8	68.6	0.23	0.25	1194	0.61	-0.38
CYMB1714-03	92.2	75.4	69.1	0.20	0.26	1195	0.65	-0.36

21699356, 2023, 4, Downloaded from https://agupubs.onlinelibrary.wiley.com/doi/10.1029/2022JB025008 by CAS - Chengdu Library, Wiley Online Library on [20/05/2024]. See the Terms and Conditions (https://onlinelibrary.wiley.com/terms-and-conditions) on Wiley Online Library for rules of use; OA articles are governed by the applicable Creative Commons License

Table 2
Continued

No. of olivine-chromite pairs	OlivineFo	ChromiteCr#	ChromiteMg#	Chromite TiO_2 (wt.%)	Chromite $Fe^{3+}/\sum Fe$	$T_{ol\text{-}chr}$ (℃)[a]	log fO_2 (ΔQFM)[b]	log fO_2 (ΔQFM)[c]
CYMB1714-04	91.0	74.0	66.0	0.23	0.26	1195	0.61	-0.27
CYMB1714-05	92.2	76.8	68.5	0.17	0.20	1182	0.14	-0.89

[a]Temperature calculated by the equation of Li et al. (1995) based on Mg-Fe equilibrium between chromite and olivine. [b]Oxygen fugacity calculated by the olivine-chromite oxybarometer of Ballhaus et al. (1991) at 0.1 GPa and Tol-chr. Note that the result is recalculated from the QFM buffer of O'Neill (1987) used in Ballhaus et al. (1991) relative to QFM buffer of Frost (1991) which is used in Davis et al. (2017). [c]Oxygen fugacity after calibration of the effect of subsolidus cooling process and silica activity.

margin and Mg-Fe zonation. These observations indicate that oxygen isotopic ratios of the olivines were not modified by re-equilibration between the olivine grains and the host magma. Olivine grains in the groundmass of the lavas were also analyzed, and they yield a value of 4.9 ± 0.6 (2σ, $n = 37$), which is basically similar to the $\delta^{18}O$ of larger olivine phenocrysts within the range of uncertainty (Figure 7).

5. Discussion

The mantle peridotites in the Kokkinorotsos podiform chromite deposit of the Troodos ophiolite were formed by melt-rock reaction between ascending boninitic magmas and their surrounding peridotites (Figures 1b1 and 1b2) (Büchl et al., 2004), while the lavas in the Margi area are typical boninitic lavas in the Troodos ophiolite (Hu et al., 2021; Sobolev et al., 1991). Therefore, the Kokkinorotsos mantle peridotites and the Margi lavas provide two independent proxies into the fO_2 of the primary boninitic magmas of the Troodos ophiolite. In the following section, we first discuss the genesis of the Kokkinorotsos mantle peridotites and the Margi lavas (Section 5.1), and then we provide new constraints on fO_2 of the primary boninitic magmas using the mantle peridotites and the boninite lavas (Sections 5.2, 5.3, and 5.4), using the olivine-chromite oxybarometer of Davis et al. (2017) and of Ballhaus et al. (1991). Finally, we compare our results with those of the IBM proto-arc magmas (FABs and boninites) to examine further whether dehydration and/or melting of the incipient subducted slab or other processes (magma degassing, crustal contamination, seawater infiltration, etc.) could have modulated the redox state of the Troodos proto-arc magmas (Section 5.5).

5.1. Petrogenesis and Relationships Between Lavas and Mantle Peridotites

Melt inclusions hosted by olivine phenocrysts of the Margi pillow lavas possess a typical boninitic composition (Figures 3a and 3b) (Hu et al., 2021). They have been considered as representative of parental magmas of boninitic lavas in the Troodos ophiolite, as they share similar Ti_8, Si_8, and trace element compositions with the Troodos boninitic lavas (Figure 3) (Hu et al., 2021; Sobolev et al., 1991). Though the whole-rock composition of Margi porphyritic lavas is out of the compositional range of boninites due to accumulation of olivine phenocrysts, the composition of the host lavas, calculated as phenocryst free using the approach of Nicklas et al. (2018) based on regression of the relationship between MgO and other elements, has low TiO_2 (0.43 ± 0.05 wt.%) and high MgO (15.3 ± 1.7 wt.%) and SiO_2 (51.9 ± 1.2 wt.%), within the range of boninites (Figures 3a and 3b). Such results imply that the host magma of the olivine phenocrysts is likely boninitic. Trace element compositions of the whole-rock of the Margi lavas are similar to those of the olivine-hosted melt inclusions and of the boninites in the Troodos ophiolite (Figure 3c). Therefore, the Margi pillow lavas are clearly part of the UPL, and high-Fo olivine phenocrysts and chromite inclusions crystallized in the earliest stage of boninitic magma fractionation.

Formation of podiform chromite deposits is related to melt-rock reaction in the mantle. Melt-rock reactions between magmas and mantle peridotites produce depleted harzburgites and dunites, and shift the magma toward a composition enriched in SiO_2 and oversaturated in chromium (Arai & Yurimoto, 1994; M. F. Zhou et al., 1994). Boninites have been widely accepted as parental magmas of high-Cr podiform chromite deposits (Cr# of ores >60) (Arai & Miura, 2016; P. F. Zhang et al., 2016; M. F. Zhou et al., 2014). For the Kokkinorotsos high-Cr podiform chromite deposit of the Troodos ophiolite, Büchl et al. (2004) have shown that (a) platinum group element (PGE) distribution patterns of dunites and chromitites are complementary, and (b) Os, Ir, Ru, and Cr concentrations decrease systematically from harzburgites to dunites. This variation of PGE is best explained by sulfide removal during percolation and reaction of a sulfur-undersaturated magma, most likely of boninitic composition (Büchl et al., 2004; M. F. Zhou et al., 1998).

21699356, 2023, 4, Downloaded from https://agupubs.onlinelibrary.wiley.com/doi/10.1029/2022JB025008 by CAS - Chengdu Library, Wiley Online Library on [20/05/2024]. See the Terms and Conditions (https://onlinelibrary.wiley.com/terms-and-conditions) on Wiley Online Library for rules of use; OA articles are governed by the applicable Creative Commons License

Table 3
Whole-Rock Compositions of the Margi Lavas of the Troodos Ophiolite, Cyprus

Sample no.	CYMB1702	CYMB1708	CYMB1709	CYMB1711	CYMB1713	CYMB1714
Major element (wt.%)						
SiO_2	44.28	44.74	43.65	41.50	45.57	43.76
TiO_2	0.18	0.19	0.17	0.14	0.24	0.21
Al_2O_3	5.61	5.73	5.05	4.56	7.04	6.08
Cr_2O_3	0.40	0.40	0.46	0.41	0.34	0.39
TFe_2O_3	8.94	8.98	9.29	8.74	9.08	9.19
MnO	0.14	0.14	0.15	0.13	0.15	0.15
MgO	33.3	32.2	34.2	33.6	28.4	31.9
CaO	3.86	4.38	3.90	5.22	5.33	4.16
Na_2O	0.44	0.59	0.48	0.42	0.70	0.41
K_2O	0.19	0.12	0.10	0.10	0.18	0.13
NiO	0.16	0.14	0.16	0.16	0.12	0.14
P_2O_5	0.01	0.01	0.01	0.01	0.01	0.01
LOI	3.37	3.16	3.22	5.05	3.75	4.02
Trace element (ppm)						
Li	27.9	22.7	22.2	23.7	23.7	37.1
Cr	3,110	2,890	3,390	3,310	2,610	3,090
V	88.0	87.0	79.0	69.0	112	90.0
Co	96.2	92.0	99.7	96.7	82.4	90.2
Ni	1,270	1,115	1,265	1,240	957	1,080
Cu	37.5	38.2	34.4	30.8	45.1	40.7
Zn	56.0	53.0	56.0	53.0	55.0	55.0
Rb	4.9	4.0	4.6	3.5	4.8	3.7
Sr	45.3	43.5	32.3	46.2	47.8	28.4
Y	5.1	5.4	4.8	4.8	6.6	6.0
Zr	11.4	14.6	15.4	9.1	15.8	13.4
Nb	0.30	0.40	0.50	0.30	0.50	0.40
Cs	0.19	0.14	0.35	0.15	0.17	0.24
Ba	11.8	8.70	7.70	4.7	19.1	7.60
La	0.30	0.40	0.50	0.30	0.70	0.60
Ce	1.20	1.30	1.50	1.10	1.90	1.70
Pr	0.20	0.22	0.22	0.19	0.28	0.25
Nd	1.20	1.30	1.20	1.10	1.60	1.40
Sm	0.49	0.50	0.44	0.37	0.59	0.49
Eu	0.12	0.16	0.15	0.14	0.21	0.18
Gd	0.62	0.70	0.61	0.66	0.87	0.69
Tb	0.12	0.14	0.12	0.12	0.17	0.13
Dy	0.83	0.92	0.81	0.79	1.16	0.89
Ho	0.19	0.21	0.19	0.18	0.27	0.21
Er	0.57	0.61	0.57	0.51	0.78	0.64
Tm	0.09	0.09	0.09	0.08	0.12	0.10
Yb	0.59	0.59	0.59	0.52	0.76	0.66

21699356, 2023, 4, Downloaded from https://agupubs.onlinelibrary.wiley.com/doi/10.1029/2022JB025008 by CAS - Chengdu Library, Wiley Online Library on [20/05/2024]. See the Terms and Conditions (https://onlinelibrary.wiley.com/terms-and-conditions) on Wiley Online Library for rules of use; OA articles are governed by the applicable Creative Commons License

Table 3
Continued

Sample no.	CYMB1702	CYMB1708	CYMB1709	CYMB1711	CYMB1713	CYMB1714
Lu	0.09	0.09	0.09	0.08	0.12	0.10
Hf	0.30	0.30	0.40	0.30	0.50	0.50
Th	0.08	0.09	0.09	0.05	0.08	0.08

Chromite in peridotites is a critical indicator of mantle processes (Dick & Bullen, 1984; Pearce et al., 2000). Mantle melting can increase Cr# of chromite in the mantle residue by extracting Al from chromite to magmas (Arai, 1994; Dick & Bullen, 1984; Hellebrand et al., 2001), and decrease concentrations of incompatible trace elements, for example, Ti. In the Cr#-TiO_2 diagram (Figure 6b), the chromite of the harzburgites and dunites examined in this study forms a positive trend that contrasts with the one expected from mantle melting. This positive relationship has been interpreted as a result of melt-rock reaction, in that exchanges with a percolating magma raises the Cr# values and TiO_2 concentrations of chromite in peridotites simultaneously (Pearce et al., 2000). Chromites in boninites plot at the righthand end of the melt-rock reaction trend in the Cr#-TiO_2 diagram (Figure 6b), further confirming that the percolating magma was boninitic in composition (Pearce et al., 2000)

Looking further at the potential for trace elements in chromite to distinguish different igneous processes, batch melting of depleted mantle was modeled after Workman and Hart (2005), with distribution coefficients from Le Roux et al. (2015), and the melting equation (0.571 Opx + 0.735 Cpx + 0.041 Chr = 0.347 Ol + 1 liquid; 1.25 Opx = 0.25 Ol + 1 liquid) from Wasylenki et al. (2003) and Parman and Grove (2004). The model predicts that, during mantle melting, both Ti and V in spinels decrease (Figure 6c); whereas Sc in chromites increases at first, and then decreases when clinopyroxene is exhausted in the mantle residue (Figure 6d). In the Ti-V and Ti-Sc diagrams, the harzburgites and dunites together form positive trends that contrast with the melting trends. Moreover, chromites in the boninites plot as endmembers of peridotite trends (Figures 6c and 6d). The simplest explanation is the interaction of the peridotites with a boninitic magma, raising Ti and V concentrations and reducing Sc concentrations in chromite simultaneously.

Therefore, together with previous studies, compositions of chromite in the Kokkinorotsos peridotites of the Troodos ophiolite strongly suggest that the harzburgites and dunites in this study were formed by progressive reactions with boninitic magmas (Figure 1b). The variations of fO_2 from harzburgites to dunites can thus provide key insights regarding the fO_2 of the primary boninitic magmas at mantle depths.

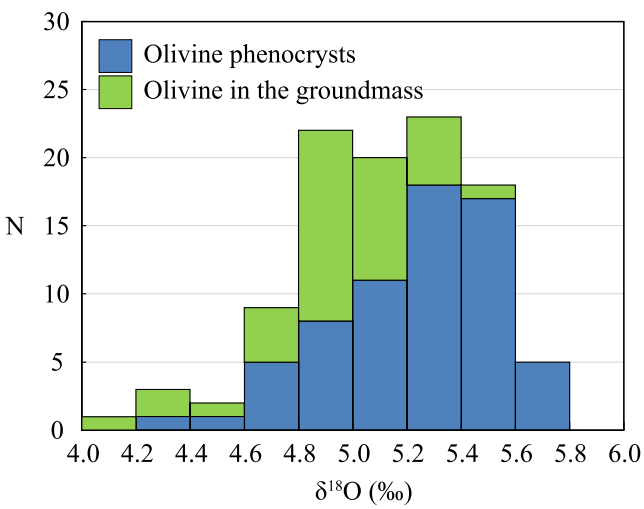

Figure 7. Oxygen isotope composition of olivine phenocrysts and olivine grains in the groundmass of the Margi pillow lavas of the Troodos ophiolite. The oxygen isotopic ratios of the olivine phenocrysts and olivine grains in the groundmass overlap.

5.2. Oxygen Fugacity of Mantle Peridotites

5.2.1. Oxygen Fugacity of Harzburgites

Oxygen fugacity of the harzburgites can be calculated based on the fayalite oxidation reaction (Ballhaus et al., 1991; Mattioli & Wood, 1988; Nikolaev et al., 2016; O'Neill & Wall, 1987; Wood & Virgo, 1989):

$$3Fe_2SiO_4\ (\text{fayalite}) + O_2 = 3SiO_2\ (\text{liquid}) + 2Fe_3O_4\ (\text{magnetite}) \quad (2)$$

where silica activity a_{SiO_2} in liquid is controlled by the reaction

$$Mg_2SiO_4\ (\text{forsterite}) + SiO_2\ (\text{liquid}) = Mg_2Si_2O_6(\text{enstatite}) \quad (3)$$

In this study, an updated olivine-orthopyroxene-chromite oxybarometer established by Davis et al. (2017) is used to calculate the fO_2 of the harzburgites. The olivine-chromite geothermometer of J. P. Li et al. (1995) is employed to calculate mantle temperatures, because it uses the same elements (Mg and Fe) and minerals (olivine and chromite) as the oxybarometer. Assuming that pressure for closure of Mg-Fe exchange in peridotites is 0.6 GPa, which is suitable for proto-arc mantle peridotites now observed in modern fore-arcs according to Birner et al. (2017), the geothermometer yields temperatures of 849–888°C for the harzburgites (Table 4).

21699356, 2023, 4, Downloaded from https://agupubs.onlinelibrary.wiley.com/doi/10.1029/2022JB025008 by CAS - Chengdu Library, Wiley Online Library on [20/05/2024]. See the Terms and Conditions (https://onlinelibrary.wiley.com/terms-and-conditions) on Wiley Online Library for rules of use; OA articles are governed by the applicable Creative Commons License

Table 4
Summary of Calculated Results for Mantle Peridotites From the Troodos Ophiolite, Cyprus

		Closure condition		Source condition 1 (1.5 Gpa, 1,400°C)		Source condition 2 (1.0 Gpa, 1,375°C)		Source condition 3 (0.6 Gpa, 1,355°C)	
		log fO_2 (ΔQFM)[b]	log fO_2 (ΔQFM)[c]	log fO_2 (ΔQFM)[d]	log fO_2 (ΔQFM)[e]	log fO_2 (ΔQFM)[d]	log fO_2 (ΔQFM)[e]	log fO_2 (ΔQFM)[d]	log fO_2 (ΔQFM)[e]
Sample	$T_{ol\text{-}chr}$ (°C)[a]	Davis et al. (2017)	Ballhaus et al. (1991)	Davis et al. (2017)	Ballhaus et al. (1991)	Davis et al. (2017)	Ballhaus et al. (1991)	Davis et al. (2017)	Ballhaus et al. (1991)
Harzburgite									
CY-H5	855	0.31	0.21	−0.58	−0.66	−0.39	−0.47	−0.24	−0.32
CY-H6	871	0.11	−0.03	−0.75	−0.88	−0.57	−0.70	−0.42	−0.54
CY-H7	888	−0.72	−0.89	−1.57	−1.73	−1.39	−1.54	−1.24	−1.39
CY-H8	860	0.29	0.23	−0.59	−0.63	−0.40	−0.44	−0.25	−0.29
CY-H9	855	−0.62	−0.96	−1.57	−1.85	−1.38	−1.67	−1.23	−1.51
CY-H10	849	0.30	0.19	−0.59	−0.69	−0.40	−0.50	−0.25	−0.35
CY-H11	861	0.13	0.05	−0.75	−0.82	−0.57	−0.63	−0.42	−0.48
Dunite									
CY-D3	859	–	0.41	–	−0.50	–	−0.65	–	−0.92
CY-D5	856	–	0.42	–	−0.50	–	−0.65	–	−0.92
CY-D6	878	–	−0.01	–	−0.90	–	−1.05	–	−1.32
CY-D7	875	–	0.46	–	−0.42	–	−0.57	–	−0.83
CY-D8	879	–	0.35	–	−0.55	–	−0.69	–	−0.96
CY-D9	858	–	0.84	–	−0.02	–	−0.17	–	−0.43
CY-D10	854	–	0.51	–	−0.37	–	−0.52	–	−0.78
CY-D11	861	–	1.00	–	0.10	–	−0.05	–	−0.32
CY-D13	873	–	1.28	–	0.40	–	0.25	–	−0.01
CY-D14	852	–	0.95	–	0.01	–	−0.14	–	−0.40
CY-D16	877	–	0.77	–	−0.11	–	−0.26	–	−0.53

[a]Temperature calculated by the equation of J. P. Li et al. (1995) based on Mg-Fe equilibrium between chromite and olivine. [b]Oxygen fugacity calculated by the olivine-orthopyroxene-chromite oxybarometer of Davis et al. (2017) at 0.6 GPa and $T_{ol\text{-}chr}$. [c]Oxygen fugacity calculated by the olivine-chromite oxybarometer of Ballhaus et al. (1991) at 0.6 GPa and $T_{ol\text{-}chr}$. Note that the result is recalculated from the QFM buffer of O'Neill (1987) used in Ballhaus et al. (1991) relative to QFM buffer of Frost (1991) in Davis et al. (2017). [d]Oxygen fugacity after calibration of the effect of subsolidus cooling process, by using the olivine-orthopyroxene-chromite oxybarometer of Davis et al. (2017). [e]Oxygen fugacity after calibration of the effect of subsolidus cooling process and silica activity, by using the olivine-orthopyroxene-chromite oxybarometer of Ballhaus et al. (1991).

Calculated fO_2 of the Troodos harzburgites is ΔQFM −0.03 ± 0.45 (where QFM represents the quartz-fayalite-magnetite buffer) (Table 4 and Figure 8a), which is slightly lower than abyssal peridotites (ΔQFM 0.31 ± 0.73) (Cottrell et al., 2021), but similar to the fO_2 values of some un-oxidized harzburgites from the Tonga Trench (ΔQFM −0.15 ± 0.44) (Birner et al., 2017) and to those of the Conical Seamount of the IBM forearc (ΔQFM −0.14 ± 0.43) (Parkinson & Pearce, 1998). In addition, the calculated fO_2 of the harzburgites roughly correlates positively with Cr# of chromite, which is an indicator of the degree of melt-rock reaction (Figure 8b).

The calculated temperatures (849–888°C) are clearly lower than the temperatures relevant to melt-rock interaction, due to diffusion of elements (i.e., Mg and Fe) between minerals during subsolidus cooling. This subsolidus re-equilibration process would also have changed the activities of the endmembers in Equation 2, which may compromise the estimated fO_2 values. Therefore, whether such results represent the true fO_2 under mantle conditions has been questioned by previous studies (Ballhaus, 1993; Birner et al., 2018; Bucholz & Kelemen, 2019; Woodland et al., 1996).

To correct the effects of subsolidus cooling, it is first necessary to constrain the P-T conditions and the initial mineral compositions that are relevant to harzburgite formation. Based on experiments and phase equilibria

21699356, 2023, 4, Downloaded from https://agupubs.onlinelibrary.wiley.com/doi/10.1029/2022JB025008 by CAS - Chengdu Library, Wiley Online Library on [20/05/2024]. See the Terms and Conditions (https://onlinelibrary.wiley.com/terms-and-conditions) on Wiley Online Library for rules of use; OA articles are governed by the applicable Creative Commons License

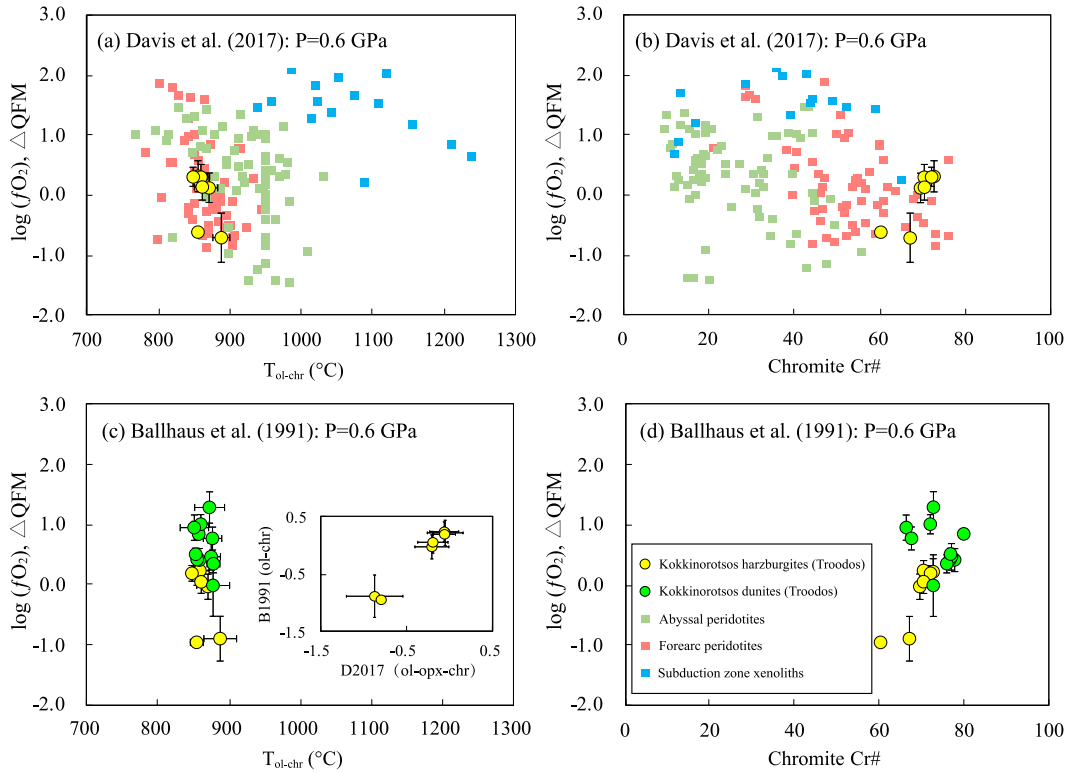

Figure 8. (a) Oxygen fugacity (fO_2) and temperatures of the harzburgites in the Troodos ophiolite. Temperature was calculated using the geothermometer of J. P. Li et al. (1995), and fO_2 was calculated following the approach of Davis et al. (2017). (b) Relationship between Cr# of chromite and fO_2 in the harzburgites in the Troodos ophiolite. Data source for abyssal peridotites are from Bryndzia and Wood (1990) and Birner et al. (2018), for subduction xenoliths from Wood and Virgo (1989) and Parkinson et al. (2003); for fore-arc peridotites from Parkinson and Pearce (1998), Pearce et al. (2000), and Birner et al. (2017). Literature data prior to 2017 were recalculated by Birner et al. (2017), using the thermometer and oxybarometer at the same pressure (0.6 GPa) as in this study. (c) Relationship between temperature and fO_2 calculated by the oxybarometer of Ballhaus et al. (1991). The inset diagram compares the calculated results using the oxybarometers of Davis et al. (2017) (D2017) to those of Ballhaus et al. (1991) (B1991). (d) Relationship between Cr# of chromite and fO_2 calculated by the oxybarometer of Ballhaus et al. (1991). The uncertainties of $T_{ol\text{-}chr}$ and fO_2 values, as shown by the error bars, were calculated using Monte Carlo simulations (n = 5,000) for each sample.

studies, the primary boninitic magmas of the Troodos ophiolite formed at 1400°C and 1.5 GPa (Falloon & Danyushevsky, 2000; Hu et al., 2021). Modal abundances of olivine, orthopyroxene, and chromite are set at 70%, 28%, and 2%, respectively, and the distribution of elements was adjusted until the equilibrium temperature reaches 1400°C at 1.5 GPa, following the method of Birner et al. (2018), which involves Mg^{2+}-Fe^{2+} exchange between olivine and chromite, and Cr^{3+}-Al^{3+} exchange between orthopyroxene and chromite. The fO_2 of the Troodos harzburgites at 1400°C and 1.5 GPa is ΔQFM −0.91 ± 0.46, about 0.9 log units lower than the fO_2 value under closure conditions (ΔQFM −0.03 ± 0.45, at 0.6 GPa and 849–888°C) (Table 4) (Figure 9a). This result is similar to those of Birner et al. (2018), in that a decrease of 120°C could cause an increase of fO_2 by 0.15–0.20 QFM log units. Notably, the positive correlation between fO_2 and chromite Cr# still exists after correction (Figure 9a), implying that fO_2 has been raised during melt-rock reaction.

However, 1400°C and 1.5 GPa can only represent extreme P-T conditions with respect to the Troodos harzburgites. Under the formation conditions of the Troodos boninitic magmas (1400°C and 1.5 GPa), the melt-rock reaction involving consumption of orthopyroxene and production of olivine would not take place because the silica activity (a_{SiO_2}) of the primary boninitic magma is close to that of the En-Fo buffer, i.e., the magma is in equilibrium with a harzburgite residue (Figure 10a). With decreasing pressure during magma ascent, the phase volume of olivine expands relative to orthopyroxene, reflected by the negative correlation between a_{SiO_2} of the En-Fo buffer and pressure. In comparison, the a_{SiO_2} of the ascending magma stays relatively constant, and this contrast would cause the interaction between the ascending magma and surrounding mantle peridotites to produce harzburgites

21699356, 2023, 4, Downloaded from https://agupubs.onlinelibrary.wiley.com/doi/10.1029/2022JB025008 by CAS - Chengdu Library, Wiley Online Library on [20/05/2024]. See the Terms and Conditions (https://onlinelibrary.wiley.com/terms-and-conditions) on Wiley Online Library for rules of use; OA articles are governed by the applicable Creative Commons License

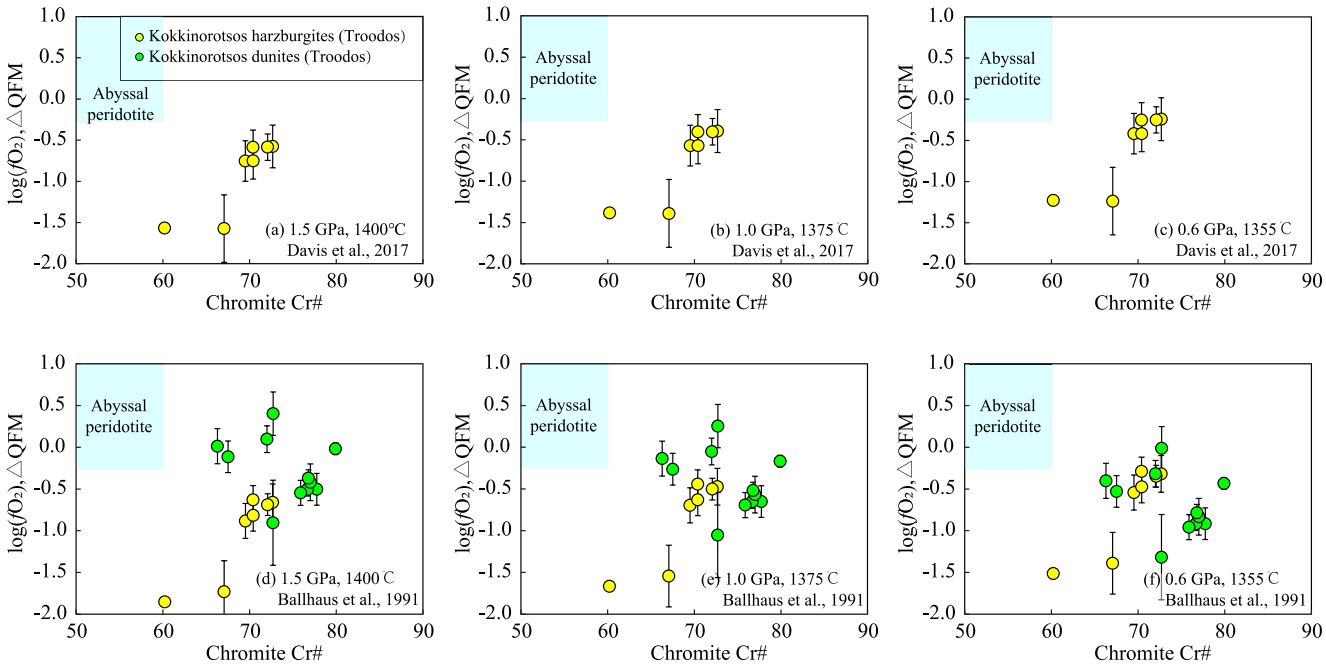

Figure 9. Chromite Cr# versus fO_2 of the mantle peridotites of the Troodos ophiolite after projection to different mantle conditions using the chromite-olivine oxybarometers of (a–c) Davis et al. (2017) and of (d–f) Ballhaus et al. (1991). The range in fO_2 of the abyssal peridotites (ΔQFM 0.31 ± 0.73) is after Cottrell et al. (2021). Error bars represent the uncertainty propagated from the analytical errors, calculated using a Monte Carlo simulation (n = 5,000) for each sample.

and dunites (Figure 10a). Given the relationship between a_{SiO_2} and liquidus P-T, fO_2 can be back-calculated to possible melt-rock reaction conditions (1375°C and 1.0 GPa), and also to 1355°C and 0.6 GPa, where 0.6 GPa is the assumed closure pressure for Mg-Fe exchange between minerals. The calculated fO_2 of the harzburgites decreases slightly with increasing pressure and temperature (1.0 GPa and 1375°C: ΔQFM −0.73 ± 0.45; 0.6 GPa and 1355°C: ΔQFM −0.58 ± 0.45), whereas fO_2 and chromite Cr# remains positively correlated (Figures 8b and 8c). Such a result also means that the uncertainty of adopted P-T conditions relevant to melt-rock interaction does not significantly change the estimated fO_2 values of the examined harzburgites.

5.2.2. Determination of fO_2 of the Dunites

For most mantle peridotites that have high Mg#, the ratio of activity of enstatite (En) in orthopyroxene, a_{en}^{opx}, to that of forsterite (Fo) in olivine, a_{fo}^{ol}, are close to 1. Accordingly, Ballhaus et al. (1991) suggested that the effect of a_{en}^{opx} could be canceled by that of a_{fo}^{ol}, and developed a simplified oxybarometer that only requires the compositions of olivine and chromite without orthopyroxene. For peridotites that contain olivine, orthopyroxene and chromite, this oxybarometer yields reasonable results comparable to other olivine-orthopyroxene-chromite oxybarometers (Ballhaus et al., 1991). It produces almost the same fO_2 results (ΔQFM −0.17 ± 0.52) as the oxybarometer of Davis et al. (2017) (ΔQFM −0.03 ± 0.45) for harzburgites of this study (Figure 8c), but suggests higher fO_2 values for the dunites (ΔQFM 0.63 ± 0.37) (Table 4). However, the oxybarometer of Ballhaus et al. (1991) is strictly valid only if the a_{SiO_2} is buffered by olivine and orthopyroxene. For dunites that do not contain orthopyroxene, this method would overestimate a_{SiO_2}, and consequently overestimate fO_2 (Equation 3; Ballhaus et al., 1991; Bucholz & Kelemen, 2019). Thus, fO_2 values of dunites calculated via this method (ΔQFM 0.63 ± 0.37) can only provide maximum estimates, unless additional correction of a_{SiO_2} is performed.

Clearly, two critical issues must be addressed when using the olivine-chromite oxybarometer of Ballhaus et al. (1991) to recover the fO_2 conditions of dunites during the melt-rock interaction. The first is the effect of subsolidus re-equilibration as is the case for the harzburgites. In dunites, Mg^{2+}-Fe^{2+} diffusion is important, but Cr^{3+}-Al^{3+} diffusion is negligible (e.g., Bucholz & Kelemen, 2019). Here, we set modal abundances of olivine and chromite to 95% and 5%, respectively, and then we re-adjusted the distribution of elements until the equilibrium temperature reached the same conditions as the harzburgites. Correction for the subsolidus effect also leads to a decrease of fO_2. The second issue is related to reduced a_{SiO_2}. According to Equation 3, deviation from the En-Fo silica buffer of 0.1 log units in the a_{SiO_2} propagates to 0.3 log units shift in fO_2. The dunites represent

21699356, 2023, 4, Downloaded from https://agupubs.onlinelibrary.wiley.com/doi/10.1029/2022JB025008 by CAS - Chengdu Library, Wiley Online Library on [20/05/2024]. See the Terms and Conditions (https://onlinelibrary.wiley.com/terms-and-conditions) on Wiley Online Library for rules of use; OA articles are governed by the applicable Creative Commons License

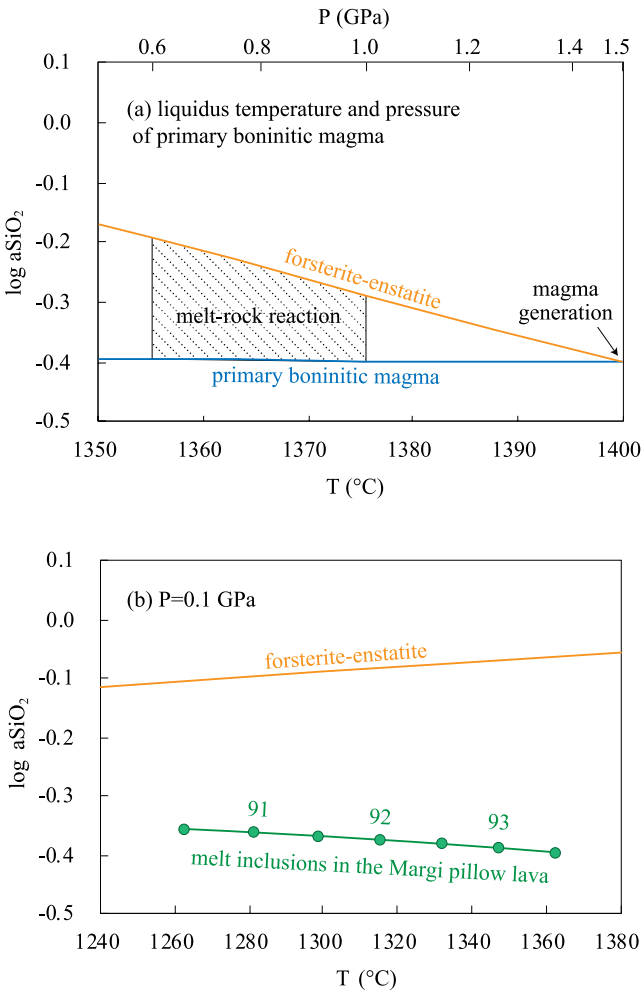

Figure 10. (a) Silica activity (a_{SiO_2}) of the Troodos primary boninitic magmas calculated by the MELTS supplemental calculator of Ghiorso and Sack (1995), in comparison with the theoretical a_{SiO_2} at the En-Fo buffer of Nicholls et al. (1971) at different liquidus temperatures and pressures during magma ascent from 1.5 GPa to 1400°C. (b) a_{SiO_2} of the parental magmas of the Margi olivines calculated by the MELTS supplemental calculator of Ghiorso and Sack (1995), in comparison with the theoretical a_{SiO_2} at En-Fo buffer of Nicholls et al. (1971) at different liquidus temperatures and 0.1 GPa. The parental magma compositions were estimated using the relationship between the compositions of melt inclusions and Fo of the host olivine phenocrysts (Figure S3 in Supporting Information S1), and the temperatures estimated using the software rhyolite-MELTS (Figure S4 in Supporting Information S1) (Gualda et al., 2012), assuming an average water content of ~2 wt.% according to studies of boninitic, olivine-hosted melt inclusions (1.38–2.12 wt.% H_2O) and fresh boninitic glasses (1.7–2.7 wt.% H_2O) in the Troodos ophiolite (Sobolev & Chaussidon, 1996; Woelki et al., 2020). The numbers (e.g., 91, 92, and 93) represent Fo values of the olivine crystallized from the parental magmas.

products of melt passage in the stable magma channel (Figure 1b1), and they were in equilibrium with the ascending primary boninitic magma. Thus, the effect of a_{SiO_2} on fO_2 can be corrected after comparison of the a_{SiO_2} of the primary boninitic magma calculated using the MELTS supplemental calculator of Ghiorso and Sack (1995) and the theoretical a_{SiO_2} at the En-Fo buffer of Nicholls et al. (1971) under P-T conditions identical to those of harzburgite (Figure 10a).

The corrected results of both harzburgites and dunites, using the oxybarometer of Ballhaus et al. (1991), are presented in Table 4 and Figures 9d–9f. At any given mantle P-T conditions, the dunites have higher fO_2 than the harzburgites. Furthermore, fO_2 tends to increase with increasing chromite Cr#, an indicator of melt-rock reaction, from harzburgites to dunites (Figure 9). These observations suggest that the fO_2 of the mantle peridotites was progressively raised during the melt-rock interaction. However, almost all the corrected fO_2 are below the QFM buffer, and none reach the range of arc lavas (1 log units above the QFM buffer; Cottrell et al., 2021). Dunites (ΔQFM −0.41 ± 0.37) and harzburgites (ΔQFM −0.85 ± 0.52) at 1.0 GPa and 1375°C of the Troodos ophiolite have lower fO_2 than that of the abyssal peridotites from the Southwest Indian Ridge (SWIR) under similar conditions (near QFM buffer at 1.25 GPa and 1320°C, according to Birner et al. (2018)) (Figure 11). These low absolute fO_2 values suggest that the increase of fO_2 during melt-rock interaction was indeed very limited during percolation of boninitic magmas in Troodos.

5.3. Oxygen Fugacity of Lavas

5.3.1. Oxygen Fugacity Calculation and Correction

To infer fO_2 of the boninitic magmas, we used the olivine-chromite oxybaromater of Ballhaus et al. (1991) that was also utilized for the Troodos dunites (Section 5.2). This approach has the main advantage of minimizing the effects of volcanic degassing and alteration (e.g., Dare et al., 2009; Evans et al., 2012), which could affect glass shards, so that any secondary processes are likely to be negligible. As such, this method has the potential to provide reliable estimates of fO_2 of the primary boninitic magmas. The Margi lavas do not contain any orthopyroxene. Therefore, like the case of the dunites, the effects of subsolidus exchange and silica activity should be considered when using this oxybaromater. Calculation and correction of fO_2 of the Margi lavas are basically consistent with those of the dunites, but there are some differences:

1. The pressure is set at 0.1 GPa for crystallization of olivine and chromite.
2. We use data of Hu et al. (2021) to build the relationship between the compositions of melt inclusions and Fo of their host olivine (Table S9 in Supporting Information S2 and Figure S3 in Supporting Information S1). For each olivine-chromite pair, the parental magma composition was then estimated on the basis of these relationships. Olivine crystallization temperatures (1,265–1354°C) were calculated by the software rhyolite-MELTS (Gualda et al., 2012) (Figure S4 in Supporting Information S1), assuming an average water content of 2 wt.%, estimated based on studies of boninitic, olivine-hosted melt inclusions (1.38–2.12 wt.% H_2O) and fresh boninitic glasses (1.7–2.7 wt.% H_2O) in the Troodos ophiolite (Sobolev & Chaussidon, 1996; Woelki et al., 2020). The a_{SiO_2} of the boninitic magmas was then calculated at the olivine crystallization temperature, and compared with the theoretical a_{SiO_2} at the En-Fo buffer of Nicholls et al. (1971) (Figure 10b).
3. The temperature calculated with the olivine–chromite geothermometer of J. P. Li et al. (1995) is about 1181 ± 21°C, that is, lower than the olivine crystallization temperature (1265–1354°C) and the tempera-

21699356, 2023, 4, Downloaded from https://agupubs.onlinelibrary.wiley.com/doi/10.1029/2022JB025008 by CAS - Chengdu Library, Wiley Online Library on [20/05/2024]. See the Terms and Conditions (https://onlinelibrary.wiley.com/terms-and-conditions) on Wiley Online Library for rules of use; OA articles are governed by the applicable Creative Commons License

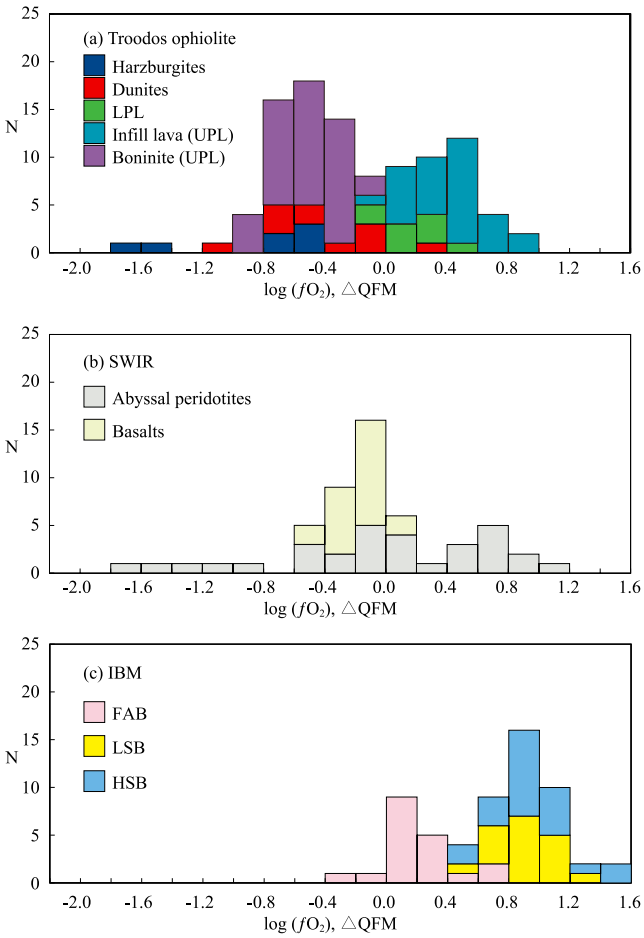

Figure 11. (a) Histogram of fO_2 of the mantle peridotites in the Troodos ophiolite after projection to mantle conditions (1.0 GPa and 1375°C) and correction of a_{SiO_2}, and the Margi lavas in the Troodos ophiolite after projection to the crystallization conditions (0.1 GPa and 1334°C) and correction of a_{SiO_2}. Recalculated fO_2 values of the LPL (Portnyagin et al., 1997) and the infill lavas in the UPL (Golowin et al., 2017; Portnyagin et al., 1996) are also presented. LPL—Lower pillow lava; UPL—upper pillow lava. The Troodos mantle peridotites and the associated magmas display MORB-like fO_2, implying that they formed under reduced conditions. (b) fO_2 values of the abyssal peridotites and basalts from the Southwest Indian Ridge at similar mantle conditions (1.25 GPa and 1320°C) (Birner et al., 2018). (c) fO_2 values of the IBM proto-arc lavas (fore-arc basalt, Low-silica boninites (LSB), and high-silica boninites (HSB), Brounce et al., 2015, 2021). The IBM proto-arc boninites (LSB and HSB) display higher redox state than the Troodos mantle peridotites and associated volcanic rocks examined in this study.

ture determined by the chromite-olivine Al exchange geothermometer (1334 ± 28°C) (Hu et al., 2021), perhaps indicating Mg-Fe exchanges between olivine and chromite during magma cooling. For each single olivine-chromite pair, fO_2 of the lavas has been back-calculated to the olivine liquidus temperature. We assume that, during the subsolidus cooling, chromite composition has changed, whereas olivine composition remained relatively constant due to its overwhelming abundance relative to chromite.

Corrected fO_2 values of the lavas are ΔQFM −0.52 ± 0.20 at the liquidus temperature, similar to the low, MORB-like fO_2 values of dunites under melt-rock reaction conditions (ΔQFM −0.41 ± 0.37, at 1.0 GPa and 1375°C), and slightly higher than those of the harzburgites (ΔQFM −0.85 ± 0.52, at 1.0 GPa and 1375°C), which were subject to lower degrees of melt-rock reaction than the dunites (Table 2 and Figure 11).

5.3.2. Limited Effects of Shallow-Level Processes on fO_2

The fO_2 of magmas can be modified by a series of processes during ascent through the crust, including magma degassing, crustal assimilation, and fractional crystallization (Cottrell et al., 2021; Lee et al., 2005, 2010; Moussallam et al., 2014, 2016, 2019; Tang et al., 2018). The effects of these processes are carefully evaluated below.

1. Fractional crystallization. It has been proposed that magma crystallization could significantly modify the fO_2 of magmas. For instance, garnet fractionation can trigger oxidation in continental arc lavas (Cao et al., 2021; Q. W. Li et al., 2021; Tang et al., 2018). However, garnet commonly crystallizes at high pressure, and its fractionation is thus favored in subduction zones with thick arc crust (>45 km thick) (Lee & Tang, 2020), whereas the crust of the Troodos ophiolite is only about 6 km thick (Abelson et al., 2001). As such, garnet is unlikely to have crystallized in the case of the Troodos ophiolite and indeed, for the Margi lavas, no garnet has yet been identified. In addition, the SI ratios of light rare earth element (LREE) to heavy REE (HREE) (i.e., LREE/HREE) and ratios of middle REE (MREE) to heavy REE (HREE) (i.e., MREE/MHREE) of the whole-rocks (e.g., La/Yb = 0.51–0.91, Dy/Yb = 1.37–1.56) and of the olivine-hosted melt inclusions (e.g., La/Yb = 0.52–1.28, Dy/Yb = 1.05–2.78) indicate that the primary boninitic magmas have not experienced garnet fractionation. Given that olivine is compatible to Fe^{2+} but incompatible to Fe^{3+}, olivine fractionation would increase the $Fe^{3+}/\sum Fe$ of the magma and consequently increase fO_2. For example, forward modeling of equilibrium crystallization of primitive MORB in a closed system using the MELTS program predicted an increase of 0.7 log units in fO_2 after extensive olivine crystallization (Ghiorso, 1997). However, the effect of olivine crystallization would be efficiently offset by crystallization of chromite, which contains a considerable portion of Fe^{3+} (Carmichael & Ghiorso, 1990; Herd, 2008). To evaluate the effects of crystallization on fO_2, we modeled a fractional crystallization system closed to oxygen, with different amounts of cotectic olivine/chromite and different initial fO_2 (Figure 12). $Fe^{3+}/\sum Fe$ in the boninitic magma was calculated following Borisov et al. (2018), with the pressure correction from H. L. Zhang et al. (2017). The compositions of crystallized olivine were determined using the Fe^{2+}-Mg partition coefficients from Putirka et al. (2007). The partition coefficient of Fe^{3+} between olivine and melt was according to Mallmann and O'Neill (2009). Fe^{3+} in chromite was empirically estimated from the correlation between Fo of olivine and Fe_2O_3 of chromite. The fractionation of the primary boninitic magmas was subsequently calculated based on the parameters above by removing olivine incrementally by 0.1% and using different cotectic olivine/chromite ratios. The results indicate a slight increase of fO_2 (<0.3 log units) during crystallization from the

21699356, 2023, 4, Downloaded from https://agupubs.onlinelibrary.wiley.com/doi/10.1029/2022JB025008 by CAS - Chengdu Library, Wiley Online Library on [20/05/2024]. See the Terms and Conditions (https://onlinelibrary.wiley.com/terms-and-conditions) on Wiley Online Library for rules of use; OA articles are governed by the applicable Creative Commons License

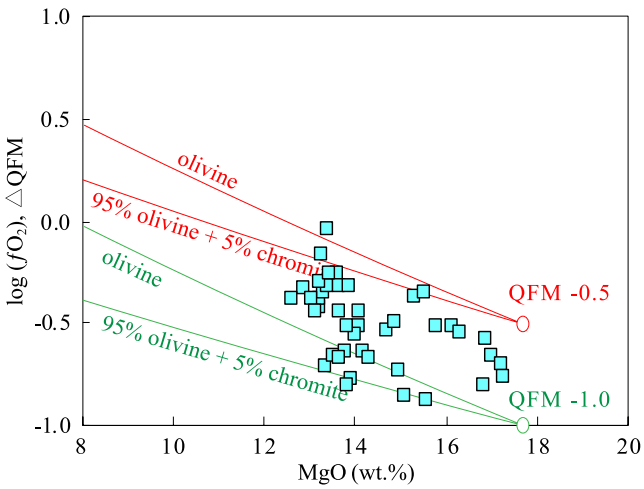

Figure 12. Corrected fO_2 value of olivine-chromite pairs in the Margi lavas of the Troodos ophiolite, in comparison with a model of variation of fO_2 during magma fractionation. The figure shows limited variations in fO_2 of the boninites during crystallization of olivine and chromite.

primary boninitic magmas to the evolved magmas, which crystallized olivine phenocrysts in the Margi lavas (Figure 12).

2. Volcanic degassing. Although magma ascent in a system closed to oxygen does not affect the fO_2 of magmas (Kress & Carmichael, 1991), theoretical calculations and investigations of natural glasses have illustrated that volcanic degassing could reduce fO_2 of the magma (Brounce et al., 2017; Burgisser & Scaillet, 2007; Kelley & Cottrell, 2012; Moussallam et al., 2014, 2016, 2019). According to gas-melt equilibrium modeled by D-Compress (Burgisser et al., 2015), Cottrell et al. (2021) illustrated that during degassing, fO_2 decreases within a limited range (<0.2 log units) until the pressure drops to ~0.25 MPa or below, after which fO_2 drops sharply. However, water content and paleobathymetric estimates from volcanic glasses suggest that the Troodos boninitic lavas were perhaps erupted at ~4–5 km depth below sealevel (Belgrano et al., 2021; Woelki et al., 2020), corresponding to hydrostatic pressures of 39~49 MPa, that is, much higher than the critical pressure for significant outgassing. Further, this study used equilibrium between early-crystallized olivine and chromite which crystallized in the deep magma plumbing system, and further minimizes the effect of degassing (Evans et al., 2012). If olivine and chromite were crystallized during magma degassing, then a decrease of fO_2 with decreasing MgO contents of the magmas would be expected. This contrasts with the observed trend (Figure 12), and thus further precludes degassing having a significant effect on magmatic fO_2 in Troodos.
3. Crustal assimilation. The Troodos ophiolite developed by near-trench spreading during subduction initiation, forming new oceanic crust just above an incipient, dehydrating subducted plate (Pearce & Robinson, 2010) (Figure 1). In other words, it is unlikely that there was nearby continental crust prior to the formation of the Troodos proto-arc magmas, and no crustal contamination. In addition, the similar oxygen isotope compositions of olivine phenocrysts and small olivine grains in the groundmass of the studied lavas from the Margi area, together with the similar trace element compositions of whole-rock and melt inclusions in olivine phenocrysts, support that crustal assimilation did not occur, and that therefore, its effect on fO_2 can be neglected.

5.4. Initial fO_2 of Primary Boninitic Magmas

The above calculations and corrections highlight several important facts:

1. Although projection to mantle conditions leads to a reduction of fO_2 values, it does not affect the positive relationship between fO_2 and chromite Cr# from the harzburgites to the dunites. The dunites, which were formed by higher degrees of melt-rock reaction than the harzburgites, also record higher fO_2 values (Figure 9).
2. The increase of fO_2 during melt-rock interaction is very limited. Almost all corrected fO_2 values are below the QFM buffer (Figure 9), and none reach the range of arc lavas and mantle xenoliths in modern subduction zones (1 log unit above the QFM buffer) (Cottrell et al., 2021) (Figure 8).
3. The boninitic lavas have similarly low, MORB-like fO_2 values under crystallization conditions (ΔQFM −0.52 ± 0.20) (Figure 11), consistent with fO_2 of the dunites (ΔQFM −0.26 ± 0.37, at 1.0 GPa and 1375°C), which represent the magma conduits of the Troodos boninitic magmas (Figure 1b1).
4. Magma ascent and other shallow-level processes, for example, degassing, assimilation, and crystallization, likely had little effects on the fO_2 of the Troodos lavas.

These observations suggest that the primary boninitic magmas in the Troodos ophiolite may not be more oxidized than MORBs, and that percolation of the boninitic magmas through the proto-arc mantle might not have raised the fO_2 to the range characterizing contemporary arc lavas (ΔQFM 1.28 ± 0.64) and peridotites from the sub-arc mantle (ΔQFM 0.96 ± 0.81; Cottrell et al., 2021). Similarly, Birner et al. (2021) showed that

21699356, 2023, 4, Downloaded from https://agupubs.onlinelibrary.wiley.com/doi/10.1029/2022JB025008 by CAS - Chengdu Library, Wiley Online Library on [20/05/2024]. See the Terms and Conditions (https://onlinelibrary.wiley.com/terms-and-conditions) on Wiley Online Library for rules of use; OA articles are governed by the applicable Creative Commons License

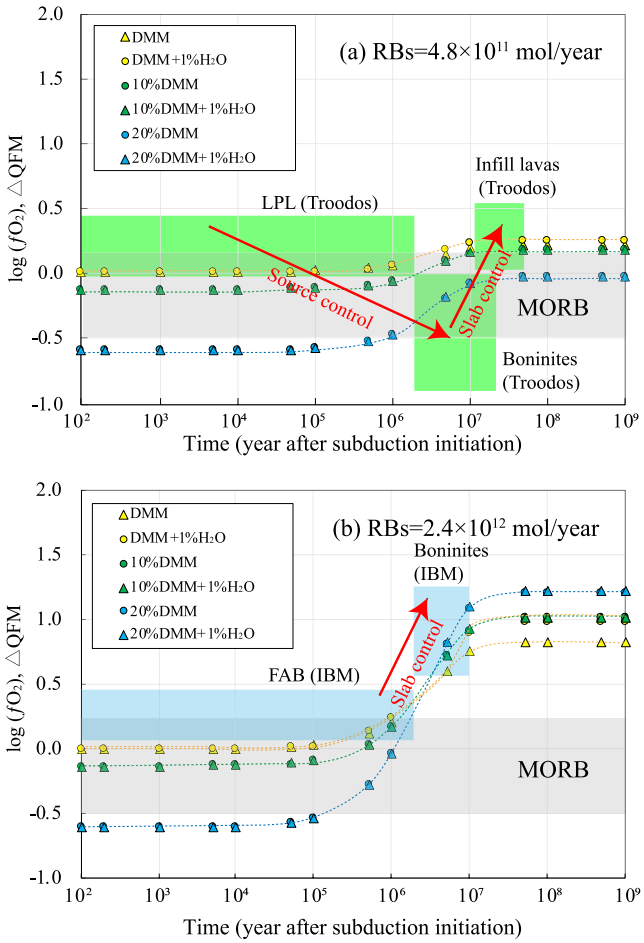

Figure 13. Evolution of fO_2 of proto-arc mantle from Troodos (a) and Izu-Bonin-Mariana (IBM) (b) with time, using different redox budget fluxes (RBs) and mantle mixing scenarios, after the models of Evans and Tomkins (2011). We first used the software alphaMELTs to simulate fO_2 variations during anhydrous and fO_2-unbuffered melting of a depleted mantle source of MORBs (DMM; Workman & Hart, 2005) at 1.5 GPa with initial fO_2 of ΔQFM = 0 (Figure S5 in Supporting Information S1). Then, mantle with different degrees of melting (0%, 10%, and 20%) were selected as starting mantle compositions to mix with different RBs. The fO_2 value and the timescale of lavas in the IBM forearc and the Troodos ophiolite are also displayed in (a) and (b), respectively, in order to show that slab components added to each proto-arc mantle may contain different RBs. The fO_2 value and the timescale of the IBM forearc is after Brounce et al. (2015, 2021) and Ishizuka et al. (2011), respectively. For the Troodos ophiolite, we assume that the timing and duration of the lower pillow lavas after subduction initiation is similar to that of fore-arc basalt in the IBM forearc. The timing and duration of the boninite and the infill lavas are estimated after Osozawa et al. (2012).

percolation of low-fO_2 MORB-type melts cannot raise the fO_2 of any interacting abyssal peridotite. These low, MORB-like fO_2 are at odds with the fact that the primary magmas of the Troodos boninites captured slab inputs released during subduction initiation (Pearce & Robinson, 2010).

The comparable low, MORB-like fO_2 values recorded in the primitive boninites and the associated peridotites of the Troodos ophiolite may instead reflect the relatively reduced conditions of the proto-arc mantle source. Such reduced mantle peridotites have also been documented both in the Conical Seamount of the IBM forearc (ΔQFM −0.14 ± 0.43) (Parkinson & Pearce, 1998, recalculated by Birner et al. (2017)) and in the Tonga trench (ΔQFM −0.15 ± 0.44) (Birner et al., 2017). However, oxidized mantle peridotites have also been sampled in the Torishima Seamount of the IBM fore-arc (ΔQFM 1.17 ± 0.44) (Parkinson & Pearce, 1998, recalculated by Birner et al. (2017)) and in the Tonga trench (ΔQFM 1.67 ± 0.10) (Birner et al., 2017), indicating that redox states of the fore-arc mantle peridotites are likely heterogeneous (Birner et al., 2017). Indeed, the high fO_2 of fore-arc peridotites has been attributed to its interaction with oxidized arc-related tholeiitic melts rather than with boninites (Birner et al., 2017; Parkinson & Pearce, 1998). In the next section, we further explore the different possibilities that could explain the relatively reduced conditions of the primary boninitic magmas of Troodos.

5.5. Implications for fO_2 Variation During Subduction Initiation

To enhance our understanding of fO_2 variations of the proto-arc mantle of the Troodos subduction zone during subduction initiation, fO_2 values of the LPL and the infill lavas were calculated based on literature data, following the same method applied to the UPL boninites of this study (see Section 5.3). A detailed introduction to the calculations and corrections are provided in the supplementary documents. Our calculations suggest that the LPL might have had low fO_2 (ΔQFM 0.16 ± 0.18) comparable to that of MORBs, and that they were succeeded by boninites with more reduced fO_2 (ΔQFM −0.52 ± 0.20) and subsequently, younger infill lavas with fO_2 of ΔQFM 0.41 ± 0.25 (Figure 13a) (Table S10 in Supporting Information S2).

At present, our knowledge of the fO_2 of proto-arc magmas that formed during subduction initiation is mostly derived from investigations of fresh glass shards (FABs and boninites) sampled in the IBM fore-arc (Brounce et al., 2015, 2021). In the IBM system, the FABs that formed during subduction inception ~52–48 Ma ago (Reagan et al., 2010, 2017, 2019), have fO_2 (ΔQFM 0.26 ± 0.19) similar to that of MORBs. In contrast, the low-Si and high-Si boninites of IBM, which formed from 51 to 45 Ma, record higher fO_2 values (ΔQFM 0.94 ± 0.22) comparable to the fO_2 of IBM arc basalts (Brounce et al., 2015, 2021) (Figure 13b). Such observations indicate that fO_2 of the IBM proto-arc mantle increased rapidly to reach fO_2 values close to those of the modern arc within 1–3 Ma of subduction inception (Figure 13b) (Brounce et al., 2015, 2021). The difference in absolute fO_2 values between the Troodos ophiolite and the IBM proto-arc boninites might be due to the different methods used to calculate them (i.e., olivine-(orthopyroxene)-chromite oxybarometer used in this study versus micro X-ray absorption near edge structure (μ-XANES) spectroscopy in IBM). However, when using the same method for both Troodos and IBM, our results suggest that the redox state of the proto-arc mantle in the Troodos subduction zone varied differently to that of the IBM proto-arc mantle during subduction initiation

21699356, 2023, 4, Downloaded from https://agupubs.onlinelibrary.wiley.com/doi/10.1029/2022JB025008 by CAS - Chengdu Library, Wiley Online Library on [20/05/2024]. See the Terms and Conditions (https://onlinelibrary.wiley.com/terms-and-conditions) on Wiley Online Library for rules of use; OA articles are governed by the applicable Creative Commons License

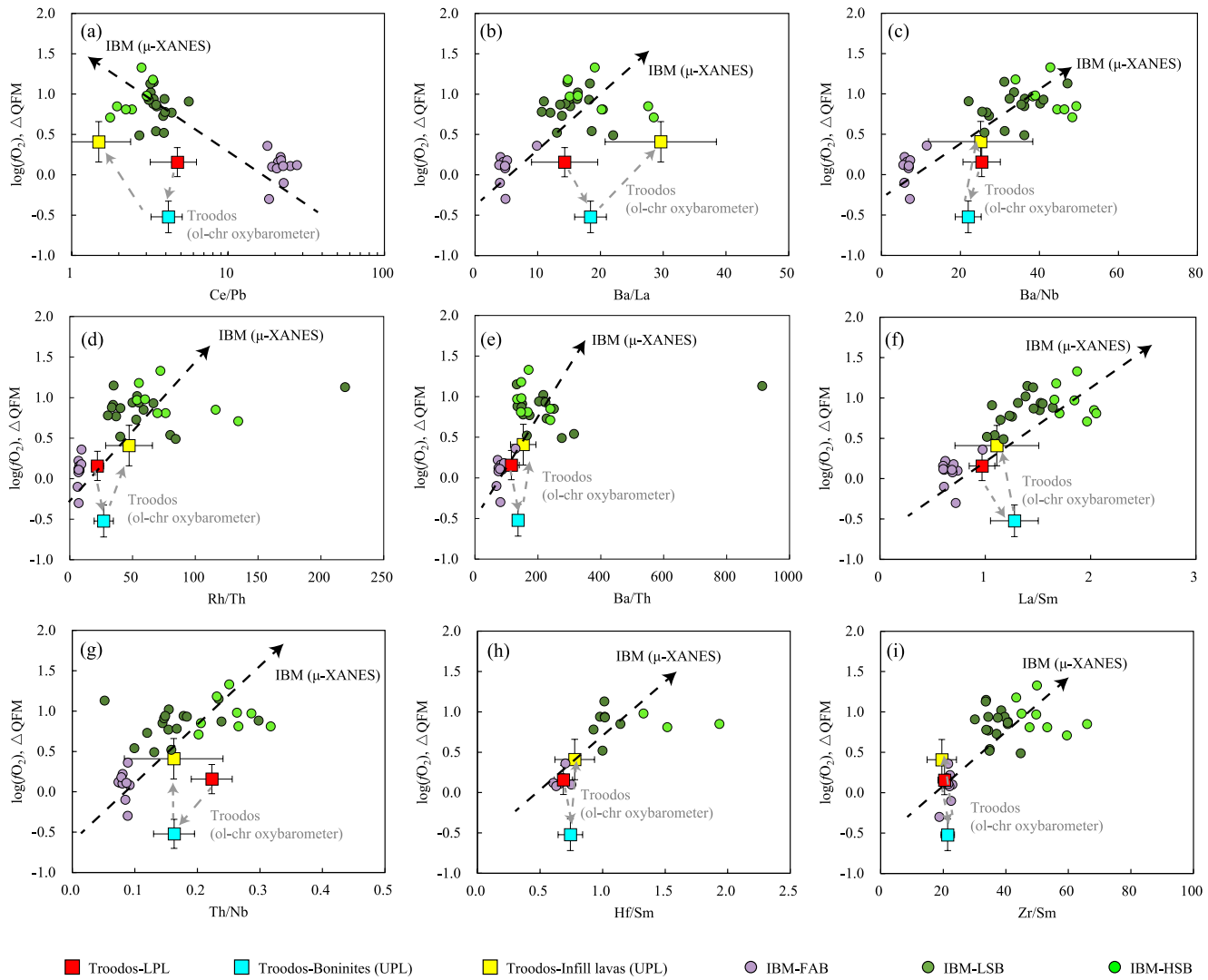

Figure 14. Relationship between fO_2 and trace element ratios of lavas. For the IBM proto-arc lavas, fO_2 values are from Brounce et al. (2021), which were calculated using in situ micro X-ray absorption near edge structure analyses on fresh glasses. Trace element compositions are from references therein. In particular, the data filtering strategy of Ribeiro et al. (2022) was further applied, only using boninites and basaltic lavas ($SiO_2 \leq 56$ wt.%) (to minimize the effects of fractionation) with a total sum of oxides equal to 100 ± 2 wt% to ensure freshness. The Troodos magmas possess lower fO_2 than the IBM boninites, despite having captured the water-rich slab fluids and the slab melts. For lavas of the Troodos ophiolite, fO_2 values are calculated in this study using the olivine-chromite oxybarometer of Ballhaus et al. (1991). Averaged trace element ratios of the Troodos lavas are estimated from the literature glass data (Pearce & Robinson, 2010; Osozawa et al., 2012; Regelous et al., 2014; Golowin et al., 2017; Woelki et al., 2018, 2019, and 2020). We also applied a similar data filtering strategy for the lavas of the Troodos ophiolite to that of Ribeiro et al. (2022), that is, using boninites and basaltic ($SiO_2 \leq 56$ wt%) LPL with a total sum of oxides equal to 100 ± 2 wt%. The arrows indicate the geochemical variations from early lavas to later lavas in the Troodos ophiolite (LPL-boninite-infill lava) and the IBM proto-arc (FAB-LSB-HSB). LPL—lower pillow lava; UPL—upper pillow lava; FAB—forearc basalts; LSB—low silica boninite; HSB—high silica boninite.

(Figures 13 and 14). As such, our new results imply that the processes that modulate the mantle oxidation state might be different in each and every subduction zone.

5.5.1. Source Versus Slab Control on the Mantle Oxidation State During Subduction Inception

Boninites are generally thought to be produced by melting of a previously depleted (10%–20% partial melting) mantle source (harzburgite) that was triggered by the release of subducted slab fluids (Falloon & Danyushevsky, 2000; Pearce & Reagan, 2019; Wood & Turner, 2009). In the Troodos ophiolite, the boninites in the UPL were likely derived from a more refractory mantle source than the mantle source of the LPL (Hu et al., 2021; Pearce & Robinson, 2010). Because partial melting in an un-buffered fO_2 system would result in

21699356, 2023, 4, Downloaded from https://agupubs.onlinelibrary.wiley.com/doi/10.1029/2022JB025008 by CAS - Chengdu Library, Wiley Online Library on [20/05/2024]. See the Terms and Conditions (https://onlinelibrary.wiley.com/terms-and-conditions) on Wiley Online Library for rules of use; OA articles are governed by the applicable Creative Commons License

a progressive decrease in fO_2 of the mantle source (Bénard et al., 2018), the decrease of fO_2 from the LPL to the UPL in the Troodos ophiolite may be attributed to a previous mantle melting event that occurred before the generation of the boninites. Modeling using the alphaMELTS program (Smith & Asimow, 2005) indicates that 20% melting could lead to a decrease of 0.6 log unit in fO_2 (Figure S5 in Supporting Information S1), which is comparable to the observed fO_2 variations between the LPL and the UPL of the Troodos ophiolite. Therefore, we propose that the decrease in fO_2 from the LPL to the UPL reveals prior mantle melting events in the source of the UPL.

Addition of slab-derived, oxidized, water-rich fluids to the sub-arc mantle has been proposed as the main reason for the high fO_2 of the IBM arc lavas (Brounce et al., 2014; Kelley & Cottrell, 2009). This model is supported by the positive correlation between fO_2 of these lavas and water-rich, slab-fluid markers (e.g., Ba/La and Ba/Nb) (Figure 14) (Brounce et al., 2021). Building upon such assumptions, the model of Evans and Tomkins (2011) was used further to investigate how fast fO_2 in the mantle source could change by adding a constant input of oxidized species from the slab, as represented by redox budget fluxes (RBs) in Figure 13. Apart from the depleted mantle source of MORBs (DMM) of Workman and Hart (2005), two other mantle sources were considered in this model to evaluate the effects of mantle depletion on fO_2: one is a depleted mantle source after extracting 10% melt with fO_2 of ΔQFM −0.1, and the other is a more depleted mantle source after 20% melting with fO_2 of ΔQFM −0.6. Our modeling results reveal that variable mantle source depletion prior to the formation of boninites may not greatly affect the rate of change of fO_2 with time (Figure 13).

5.5.2. Different Slab Inputs Between Troodos and IBM Proto-Arc Magmas

Trace element ratios of suprasubduction volcanic rocks can be used to track the addition of slab fluids into the mantle source of their magmas (Pearce et al., 2005) (Figure 15). For instance, Rb and Ba are readily extracted from the subducted slab in water-rich slab-derived fluids and sediment melts, wheareas Th and La are mobilized mainly by sediment melting (Elliott, 2003; Johnson & Plank, 1999; Keppler, 1996; Pearce et al., 2005) and Nb and Sm extracted during mantle melting (Ayers & Watson, 1993; Brenan et al., 1994; Ryerson & Watson, 1987). Thus, Rb/Th and Ba/Th can track water-rich slab fluids, Th/Nb and La/Sm can identify sediment melts, whilst Ba/Nb tracks the total slab input (Pearce et al., 2005; Ribeiro et al., 2022). In contrast, Nb and Zr are more easily mobilized than Y and Yb during mantle melting, and Nb/Yb and Zr/Y can be used to track mantle source depletion/enrichment together with the extent of mantle melting (Pearce et al., 2005). Rb/Th and Ba/Th increase from FABs to LSB and HSB in the IBM proto-arc and from LPL to boninite in the Troodos ophiolite (Figure 15a), both of which are consistent with an increasing contribution of water-rich slab fluids with time both in IBM and Troodos (Ishizuka et al., 2006; Reagan et al., 2010, 2019; Ribeiro et al., 2022). The increase in Ba/Nb and Th/Nb from the IBM FABs to LSB and HSB (Figure 15b) indicates an increased infiltration of total slab fluids and sediment melts, respectively, into the proto-arc mantle as the nascent subducted Pacific plate continued foundering. Such a trend is also observed in Troodos. The La/Sm versus Rb/Th diagram (Figure 15c) and the Nb/Yb versus Th/Nb diagram (Figure 15d) show that (a) the Troodos proto-arc magmas captured water-rich slab fluids similarly to the IBM LSB (as demonstrated by their similar Rb/Th and Ba/Th); and (b) they captured the slab-derived sediment melts similarly to the IBM LSB and HSB, as shown by their Th/Nb and La/Sm.

Hf/Sm and Zr/Sm have also been shown to change during melting of amphibolite, and thus can be used to identify slab melts generated by melting of subducted oceanic crust in the amphibolite facies (Foley et al., 2002; H. Y. Li et al., 2019; Pearce et al., 1992). In Figures 15e and 15f, the IBM proto-arc boninites display positive relationships in La/Sm versus Hf/Sm and La/Sm versus Zr/Sm, suggesting the addition of slab-derived amphibolite melts into the mantle source of these lavas (H. Y. Li et al., 2019; Ribeiro et al., 2022). In contrast, although the Troodos boninites display similar Hf/Sm to the IBM LSB (Figure 15e), they have lower Zr/Sm, suggesting that they perhaps captured the amphibolite slab melts to a lesser extent than the IBM LSB and HSB (Figure 15f).

In the Troodos ophiolite, Zr/Y decreases with decreasing Y from the LPL to the UPL (Figure 15g). This positive trend can be explained by mantle melting, because Zr and Y are relatively immobile during slab dehydration, whereas Zr is more compatible than Y during mantle melting (Brounce et al., 2014; Pearce et al., 2005). In contrast, in the IBM proto-arc lavas, Zr/Y increases with decreasing Y (Figure 15g). This is not consistent with partial melting but could instead indicate some contribution of Zr from the subducted slab to the mantle source, perhaps during melting of subducted amphibolite (H. Y. Li et al., 2019; Pearce et al., 1992). Indeed, this enrichment in Zr is associated with enrichment in LREE over MREE and HREE (e.g., La/Sm in Figure 15h), which has been attributed to addition of slab melts generated under amphibolite facies conditions (Pearce et al., 1992;

21699356, 2023, 4, Downloaded from https://agupubs.onlinelibrary.wiley.com/doi/10.1029/2022JB025008 by CAS - Chengdu Library, Wiley Online Library on [20/05/2024]. See the Terms and Conditions (https://onlinelibrary.wiley.com/terms-and-conditions) on Wiley Online Library for rules of use; OA articles are governed by the applicable Creative Commons License

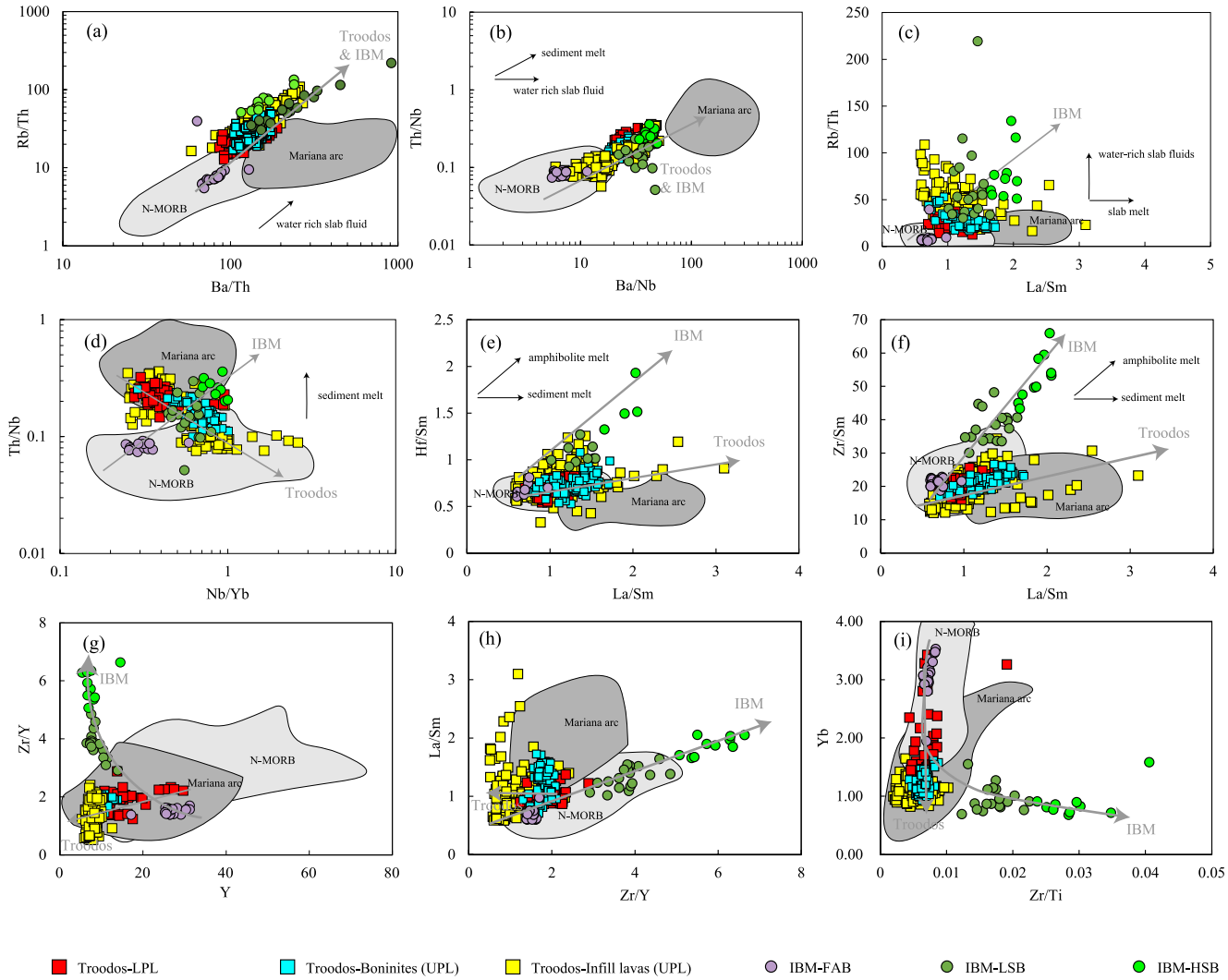

Figure 15. Trace element compositions of lavas in the Troodos ophiolite and the Izu-Bonin-Mariana (IBM) forearc. Trace element data of lavas of the IBM proto-arc are from a filtered data set of Ribeiro et al. (2022), including data from Coulthard (2018) and Coulthard et al. (2021). Trace element data of fresh volcanic glasses of the Troodos ophiolite are from literature (Pearce & Robinson, 2010; Osozawa et al., 2012; Regelous et al., 2014; Golowin et al., 2017; Woelki et al., 2018, 2019, 2020). The arrows indicate the geochemical variations from early lavas to later lavas in the Troodos ophiolite (LPL-boninite-infill lava) and the IBM proto-arc (FAB-LSB-HSB). The area of N-MORB and Mariana arc compositional fields are from Jenner and O'Neill (2012) and Ribeiro et al. (2015) and Ribeiro and Lee (2017), respectively. LPL—lower pillow lava; UPL—upper pillow lava; FAB—forearc basalts; LSB—low silica boninite; HSB—high silica boninite. Note that the Troodos boninites are similar to the IBM LSB in terms of slab-fluid markers (Ba/Th, Rb/Th, Th/Nb, La/Sm) (panels (a)–(c)), supporting the notion that the Troodos proto-arc magmas also captured the water-rich slab fluids and the slab melts released during subduction inception (e.g., Reagan et al., 2010, 2019).

Umino et al., 2015). Addition of amphibolite slab melts is also suggested by the Hf/Sm and Zr/Sm in the case of the IBM boninites (Figures 15e and 15f).

5.5.3. Possible Reasons for the Different Oxidation State Between Troodos and IBM Proto-Arc Boninites

Our study shows that the Troodos proto-arc boninites are much less oxidized than the IBM proto-arc boninites, despite both having captured the slab fluids released during subduction inception (Pearce & Robinson, 2010). This difference in the redox state of the IBM and Troodos proto-arc boninites might be explained by a number of factors:

One could be that the difference is due to shallow-level processes. For instance, volcanic degassing, interaction with seawater, hydrothermal fluids or assimilation of altered oceanic crust upon magma ascent have the potential to raise the fO_2 of magmas (e.g., Nicklas et al., 2022). However, the IBM proto-arc boninites have likely experienced minimal volcanic degassing and relatively limited interaction with hydrothermal brines,

21699356, 2023, 4, Downloaded from https://agupubs.onlinelibrary.wiley.com/doi/10.1029/2022JB025008 by CAS - Chengdu Library, Wiley Online Library on [20/05/2024]. See the Terms and Conditions (https://onlinelibrary.wiley.com/terms-and-conditions) on Wiley Online Library for rules of use; OA articles are governed by the applicable Creative Commons License

seawater and/or crustal assimilation (Brounce et al., 2015, 2021). Therefore, such secondary processes might not account for the high fO_2 values of the IBM proto-arc boninites. Indeed, Brounce et al. (2021) estimated that the fO_2 of the IBM boninitic magmas may have decreased by ~0.5 orders of magnitude if sulfur was lost to the gas phase, and so the calculated fO_2 values would only represent minimum estimates. Therefore, S degassing as well as other shallow-level processes would not account for the high fO_2 values of the IBM boninites (Brounce et al., 2021).

Building upon the assumption that slab fluids are the main oxidizing agents of subduction zone magmas, we propose that the slab subducted beneath Troodos could have released reduced species upon slab dehydration and/or slab melting, as emphasized by our modeling (Figure 13). For instance, it has been proposed that slab-derived sulfur would be one of the most important elements that could modulate the redox state of the mantle wedge, because of its valence state (from −2 to +6). Slab-derived fluids would thus carry either reduced (H_2S, HS^-) or oxidized (SO_4^{2-}) sulfur species that could reduce or oxidize the asthenospheric mantle, respectively (e.g., Chowdhury et al., 2022; Evans et al., 2012; J. L. Li et al., 2020; Tomkins & Evans, 2015). Our study emphasizes the fact that slab fluids have the potential to carry reduced species (such as carbon-, sulfur-, and iron-bearing species) upon slab dehydration and/or slab melting (Chowdhury et al., 2022; Evans & Frost, 2020; Piccoli et al., 2019), and this scenario could possibly explain the low, MORB-like oxidation state of the Troodos proto-arc magmas (Figure 13).

Lastly, we propose that the differences in the redox state between the Troodos and the IBM proto-arc boninites could also be ascribed to slab melts. For instance, higher Zr/Sm and Hf/Sm observed in the IBM LSB and HSB suggest that they both captured slab melts released from the subducted oceanic crust (Figures 15e and 15f) (H. Y. Li et al., 2019). Although the Troodos boninites display similar Hf/Sm to the IBM LSB, their lower Zr/Sm ratios in Figure 15 suggest that, perhaps, they captured slab-derived melts to a lesser extent than the IBM LSB. Slab-derived amphibolite melts may have the potential to transfer Fe^{3+}, as well as other oxidized species (e.g., SO_4^{2-}), to the proto-arc mantle wedge and further oxidize it, and lesser infiltration of such melts to the Troodos proto-arc mantle could account for the reduced redox state observed in the boninites and associated mantle rocks. However, the potential role of such slab-derived melts to oxidize or reduce the mantle source of subduction zone magmas needs to be examined further (Muth & Wallace, 2021).

6. Conclusions

This study provides new data of fO_2 of mantle peridotites and boninitic magmas of the Troodos ophiolite, Cyprus, using an olivine-chromite oxybarometer. Key findings are as follows:

Mantle peridotites in the Kokkinorotsos podiform chromite deposit of the ophiolite were formed by reaction between mantle peridotites and upward percolating boninitic magmas. Mantle dunites were formed by larger degrees of melt-rock reaction than the enclosing harzburgites. Under melt-rock reaction conditions (1.0 GPa, 1375°C), fO_2 increased slightly from the harzburgites (ΔQFM −0.85 ± 0.52) to the dunites (ΔQFM −0.41 ± 0.37). However, our results further suggest that the proto-arc mantle of Troodos had MORB-like fO_2 during subduction inception. Such values are generally lower than the $fO2$ of comparable IBM arc lavas (ΔQFM 1.28 ± 0.64) and of the fore-arc peridotites from IBM and Tonga (ΔQFM 0.96 ± 0.81), implying that the Troodos proto-arc mantle recorded relatively reduced conditions.

The boninitic lavas of the Troodos ophiolite contain large olivine phenocrysts. Previous studies of melt inclusions in these phenocrysts suggest that they crystallized from a primary boninitic magma (Hu et al., 2021; Sobolev et al., 1991). The olivine phenocrysts and chromite inclusions record low fO_2 (ΔQFM −0.52 ± 0.20) under their crystallization conditions (0.1 GPa, 1334°C). Because shallow-level processes (e.g., crystallization, assimilation, and degassing) have had limited influence on fO_2 of the Troodos proto-arc lavas, the similarly low fO_2 of mantle peridotites and the lavas suggest that the primary boninitic magma also had low, MORB-like fO_2.

Using literature data of the LPL and infill lavas of the Troodos ophiolite, we find that the redox state of the proto-arc mantle in the Troodos subduction zone evolved relatively slowly and changed little during its development, and followed a different path to that of the IBM proto-arc. There appears to have been a more reduced subduction input (either as water-rich slab fluids or slab melts) in the case of Troodos, and comparison suggests that slab-derived fluids may have variable and different redox states from one subduction zone to another. The fact

21699356, 2023, 4, Downloaded from https://agupubs.onlinelibrary.wiley.com/doi/10.1029/2022JB025008 by CAS - Chengdu Library, Wiley Online Library on [20/05/2024]. See the Terms and Conditions (https://onlinelibrary.wiley.com/terms-and-conditions) on Wiley Online Library for rules of use; OA articles are governed by the applicable Creative Commons License

that we cannot exclude the possibility that other processes may modulate the fO_2 of magmas in different subduction zones, further suggests that one model does not fit all.

Data Availability Statement

Supplementary documents to this paper are available at Figshare (https://doi.org/10.6084/m9.figshare.20155127).

Acknowledgments
Prof. Julian Pearce is sincerely thanked for guiding the chromite analysis and helpful discussions on the project. We are grateful for constructive comments by Prof. Paul T. Robinson, an anonymous reviewer and the associate editor, Prof. Fang-Zhen Teng that greatly improved the quality of the manuscript. The authors appreciate the help of Fu Xiao during EPMA analysis and Dr. Qiu-Li Li, Dr. Guo-Qiang Tang and Jiao Li during the SIMS analysis. We sincerely thank the editor, Prof. Mark Dekkers and Prof. Isabelle Manighetti, and the production team for their patience and assistance in getting the paper published. This study was supported by the National Natural Science Foundation of China (42202090 and 91962216).

References

Abelson, M., Baer, G., & Agnon, A. (2001). Evidence from gabbro of the Troodos ophiolite for lateral magma transport along a slow-spreading mid-ocean ridge. *Nature*, *409*(6816), 72–75. https://doi.org/10.1038/35051058

Arai, S. (1994). Characterization of spinel peridotites by olivine-spinel compositional relationships: Review & interpretation. *Chemical Geology*, *113*(3–4), 191–204. https://doi.org/10.1016/0009-2541(94)90066-3

Arai, S., & Miura, M. (2016). Formation and modification of chromitites in the mantle. *Lithos*, *264*, 277–295. https://doi.org/10.1016/j.lithos.2016.08.039

Arai, S., & Yurimoto, H. (1994). Podiform chromitites of the Tari-Misaka ultramafic complex, southwestern Japan, as mantle-melt interaction products. *Economic Geology*, *89*(6), 1279–1288. https://doi.org/10.2113/gsecongeo.89.6.1279

Ayers, J. C., & Watson, E. B. (1993). Rutile solubility and mobility in supercritical aqueous fluids. *Contributions to Mineralogy and Petrology*, *114*(3), 321–330. https://doi.org/10.1007/bf01046535

Bailey, D. G., Langdon, G. S., Malpas, J., & Robinson, P. T. (1991). Ultramafic and related lavas from the Margi area, Troodos ophiolite. In I. L. Gibson, J. Malpas, P. T. Robinson, & C. Xenophontos (Eds.), *Cyprus crustal study project initial report, holes CY-1 and 1a* (pp. 187–202). Geological Survey of Canada

Ballhaus, C. (1993). Redox states of lithospheric and asthenospheric upper mantle. *Contributions to Mineralogy and Petrology*, *114*(3), 331–348. https://doi.org/10.1007/bf01046536

Ballhaus, C., Berry, R. F., & Green, D. H. (1991). High pressure experimental calibration of the olivine-orthopyroxene-spinel oxygen geobarometer: Implications for the oxidation state of the upper mantle. *Contributions to Mineralogy and Petrology*, *107*(1), 27–40. https://doi.org/10.1007/bf00311183

Barnes, S. J., & Roeder, P. L. (2001). The range of spinel compositions in terrestrial mafic and ultramafic rocks. *Journal of Petrology*, *42*(12), 2279–2302. https://doi.org/10.1093/petrology/42.12.2279

Batanova, V. G., & Sobolev, A. V. (2000). Compositional heterogeneity in subduction-related mantle peridotites, Troodos massif, Cyprus. *Geology*, *28*(1), 55–58. https://doi.org/10.1130/0091-7613(2000)28<55:chismp>2.0.co;2

Belgrano, T. M., Tollan, P. M., Marxer, F., & Diamond, L. W. (2021). Paleobathymetry of submarine lavas in the Samail and Troodos ophiolites: Insights from volatiles in glasses & implications for hydrothermal systems. *Journal of Geophysical Research: Solid Earth*, *126*, e2021JB021966. https://doi.org/10.1029/2021JB021966

Bénard, A., Woodland, A. B., Arculus, R. J., Nebel, O., & McAlpine, S. R. B. (2018). Variation in sub-arc mantle oxygen fugacity during partial melting recorded in refractory peridotite xenoliths from the West Bismarck Arc. *Chemical Geology*, *486*, 16–30. https://doi.org/10.1016/j.chemgeo.2018.03.004

Birner, S. K., Cottrell, E., Warren, J. M., Kelley, K. A., & Davis, F. A. (2018). Peridotites and basalts reveal broad congruence between two independent records of mantle fO2 despite local redox heterogeneity. *Earth and Planetary Science Letters*, *494*, 172–189. https://doi.org/10.1016/j.epsl.2018.04.035

Birner, S. K., Cottrell, E., Warren, J. M., Kelley, K. A., & Davis, F. A. (2021). Melt addition to mid-ocean ridge peridotites increases spinel Cr# with no significant effect on recorded oxygen fugacity. *Earth and Planetary Science Letters*, *566*, 116951. https://doi.org/10.1016/j.epsl.2021.116951

Birner, S. K., Warren, J. M., Cottrell, E., Davis, F. A., Kelley, K. A., & Falloon, T. J. (2017). Forearc peridotites from Tonga record heterogeneous oxidation of the mantle following subduction initiation. *Journal of Petrology*, *58*(9), 1755–1780. https://doi.org/10.1093/petrology/egx072

Borisov, A., Behrens, H., & Holtz, F. (2018). Ferric/ferrous ratio in silicate melts: A new model for 1 atm data with special emphasis on the effects of melt composition. *Contributions to Mineralogy and Petrology*, *173*(12), 1–15. https://doi.org/10.1007/s00410-018-1524-8

Brenan, J. M., Shaw, H. F., Phinney, D. L., & Ryerson, F. J. (1994). Rutile aqueous fluid partitioning of Nb, Ta, Hf, Zr, U and Th: Implications for high field strength element depletions in island arc basalts. *Earth and Planetary Science Letters*, *128*(3–4), 327–339. https://doi.org/10.1016/0012-821x(94)90154-6

Brounce, M. N., Kelley, K. A., & Cottrell, E. (2014). Variations in $Fe^{3+}/\sum Fe$ of Mariana Arc basalts & mantle wedge fO_2. *Journal of Petrology*, *55*(12), 2513–2536. https://doi.org/10.1093/petrology/egu065

Brounce, M. N., Kelley, K. A., Cottrell, E., & Reagan, M. K. (2015). Temporal evolution of mantle wedge oxygen fugacity during subduction initiation. *Geology*, *43*(9), 775–778. https://doi.org/10.1130/g36742.1

Brounce, M. N., Reagan, M. K., Kelley, K. A., Cottrell, E., Shimizu, K., & Almeev, R. (2021). Covariation of slab tracers, volatiles, and oxidation during subduction initiation. *Geochemistry, Geophysics, Geosystems*, *22*(6), e2021GC009823. https://doi.org/10.1029/2021gc009823

Brounce, M. N., Stolper, E., & Eiler, J. (2017). Redox variations in Mauna Kea lavas, the oxygen fugacity of the Hawaiian plume, and the role of volcanic gases in Earth's oxygenation. *Proceedings of the National Academy of Sciences*, *114*(34), 8997–9002. https://doi.org/10.1073/pnas.1619527114

Bryndzia, L. T., & Wood, B. J. (1990). Oxygen thermobarometry of abyssal spinel peridotites: The redox state and C–O–H volatile composition of the Earth's sub-oceanic upper mantle. *American Journal of Science*, *290*(10), 1093–1116. https://doi.org/10.2475/ajs.290.10.1093

Büchl, A., Brügmann, G., & Batanova, V. G. (2004). Formation of podiform chromitite deposits: Implications from PGE abundances and Os isotopic compositions of chromites from the Troodos complex, Cyprus. *Chemical Geology*, *208*(1–4), 217–232. https://doi.org/10.1016/j.chemgeo.2004.04.013

Büchl, A., Brügmann, G., Batanova, V. G., Munker, C., & Hofmann, A. W. (2002). Melt percolation monitored by Os isotopes and HSE abundances: A case study from the mantle section of the Troodos Ophiolite. *Earth and Planetary Science Letters*, *204*(3–4), 385–402. https://doi.org/10.1016/s0012-821x(02)00977-9

Bucholz, C. E., & Kelemen, P. B. (2019). Oxygen fugacity at the base of the Talkeetna arc, Alaska. *Contributions to Mineralogy and Petrology*, *174*(10), 79. https://doi.org/10.1007/s00410-019-1609-z

21699356, 2023, 4, Downloaded from https://agupubs.onlinelibrary.wiley.com/doi/10.1029/2022JB025008 by CAS - Chengdu Library, Wiley Online Library on [20/05/2024]. See the Terms and Conditions (https://onlinelibrary.wiley.com/terms-and-conditions) on Wiley Online Library for rules of use; OA articles are governed by the applicable Creative Commons License

Burgisser, A., Alletti, M., & Scaillet, B. (2015). Simulating the behavior of volatiles belonging to the C–O–H–S system in silicate melts under magmatic conditions with the software D-Compress. *Computers & Geosciences*, *79*, 1–14. https://doi.org/10.1016/j.cageo.2015.03.002

Burgisser, A., & Scaillet, B. (2007). Redox evolution of a degassing magma rising to the surface. *Nature*, *445*(7124), 194–197. https://doi.org/10.1038/nature05509

Cao, Y., Wang, C. Y., Wei, B., & Bao, H. (2021). Mantle source and magma oxygen fugacity of Permian Ni–Cu sulfide-bearing mafic-ultramafic intrusions in the Inner Mongolia, North China: Controls on the sulfide saturation of magmas in the Andean-style continental convergent margins. *Lithos*, *390*, 106105. https://doi.org/10.1016/j.lithos.2021.106105

Carmichael, I. S. E., & Ghiorso, M. S. (1990). The effect of oxygen fugacity on the redox state of natural liquids and their crystallizing phases. *Reviews in Mineralogy*, *24*, 191–212.

Chen, Y., Niu, Y., Shen, F., Gao, Y., & Wang, X. (2020). New U-Pb zircon age and petrogenesis of the plagiogranite, Troodos ophiolite, Cyprus. *Lithos*, *362*, 105472. https://doi.org/10.1016/j.lithos.2020.105472

Chowdhury, P., Dasgupta, R., Phelps, P. R., Costin, G., & Lee, C. T. A. (2022). Oxygen fugacity range of subducting crust inferred from fractionation of trace elements during fluid-present slab melting in the presence of anhydrite versus sulfide. *Geochimica et Cosmochimica Acta*, *325*, 214–231. https://doi.org/10.1016/j.gca.2022.02.030

Christie, D. M., Carmichael, I. S. E., & Langmuir, C. H. (1986). Oxidation states of mid-ocean ridge basalt glasses. *Earth and Planetary Science Letters*, *79*(3–4), 397–411. https://doi.org/10.1016/0012-821x(86)90195-0

Cottrell, E., Birner, S., Brounce, M., Davis, F., Waters, L., & Kelley, K. (2021). Oxygen fugacity across tectonic settings. In *Magma redox geochemistry* (pp. 33–61). Wiley. https://doi.org/10.1002/ESSOAR.10502445.1

Cottrell, E., & Kelley, K. A. (2011). The oxidation state of Fe in MORB glasses & the oxygen fugacity of the upper mantle. *Earth and Planetary Science Letters*, *305*(3–4), 270–282. https://doi.org/10.1016/j.epsl.2011.03.014

Coulthard, D. A., Jr. (2018). *Subduction initiation and igneous petrogenesis: Characterizing melt generation at a new convergent boundary through the geochemical analysis of volcanic glass*. (MS thesis). University of Iowa.

Coulthard, D. A., Jr., Reagan, M. K., Shimizu, K., Bindeman, I. N., Brounce, M., Almeev, R. R., et al. (2021). Magma source evolution following subduction initiation: Evidence from the element concentrations, stable isotope ratios, and water contents of volcanic glasses from the Bonin forearc (IODP expedition 352). *Geochemistry, Geophysics, Geosystems*, *22*(1). https://doi.org/10.1029/2020GC009054

Crawford, A. J., Falloon, T. J., & Green, D. H. (1989). Classification, petrogenesis & tectonic setting of boninites. In A. J. Crawford (Ed.), *Boninites*, *1–49*. Unwin Hyman.

Dare, S. A. S., Pearce, J. A., McDonald, I., & Styles, M. T. (2009). Tectonic discrimination of peridotites using fO_2-Cr# and Ga-Ti-FeIII systematics in chrome-spinel. *Chemical Geology*, *261*(3–4), 199–216. https://doi.org/10.1016/j.chemgeo.2008.08.002

Davis, F. A., Cottrell, E., Birner, S. K., Warren, J. M., & Lopez, O. G. (2017). Revisiting the electron microprobe method of spinel-olivine-orthopyroxene oxybarometry applied to spinel peridotites. *American Mineralogist*, *102*(2), 421–435. https://doi.org/10.2138/am-2017-5823

Dick, H. J., & Bullen, T. (1984). Chromian spinel as a petrogenetic indicator in abyssal and alpine-type peridotites and spatially associated lavas. *Contributions to Mineralogy and Petrology*, *86*(1), 54–76. https://doi.org/10.1007/bf00373711

Edwards, S., Hudson-Edwards, K. A., Cann, J., Malpas, J., & Xenophontos, C. (2010). *Classic geology in Europe* (Vol. 7). Dunedin Academic Press.288 p.

Eiler, J. M., Farley, K. A., Valley, J. W., Stolper, E. M., Hauri, E., & Craig, H. (1995). Oxygen isotope evidence against bulk recycled sediment in the source of Pitcairn island lavas. *Nature*, *377*(6545), 138–141. https://doi.org/10.1038/377138a0

Elliott, T. R. (2003). Tracers of the slab. In J. Eiler (Ed.), *Inside the subduction factory*, *Geophysical monograph series* (Vol. 138, pp. 23–45).

Evans, K. A., Elburg, M. A., & Kamenetsky, V. S. (2012). Oxidation state of subarc mantle. *Geology*, *40*(9), 783–786. https://doi.org/10.1130/g33037.1

Evans, K. A., & Frost, B. R. (2020). Deserpentinization in subduction zones as a source of oxidation in arcs: A reality check. *Journal of Petrology*, *62*(1), 1–32. https://doi.org/10.1093/petrology/egab016

Evans, K. A., & Tomkins, A. G. (2011). The relationship between subduction zone redox budget and arc magma fertility. *Earth and Planetary Science Letters*, *308*(3–4), 401–409. https://doi.org/10.1016/j.epsl.2011.06.009

Falloon, T. J., & Danyushevsky, L. V. (2000). Melting of refractory mantle at 1.5, 2 and 2.5 GPa under anhydrous and H2O-undersaturated conditions: Implications for the petrogenesis of high-Ca boninites and the influence of subduction components on mantle melting. *Journal of Petrology*, *41*(2), 257–283. https://doi.org/10.1093/petrology/41.2.257

Foley, S., Tiepolo, M., & Vannucci, R. (2002). Growth of early continental crust controlled by melting of amphibolite in subduction zones. *Nature*, *417*(6891), 837–840. https://doi.org/10.1038/nature00799

Frost, B. R. (1991). Introduction to oxygen fugacity and its petrologic importance. In D. H. Lindsley (Ed.), *Oxide minerals: Petrologic and magnetic significance* (Vol. 25, pp. 1–9). Reviews in Mineralogy and Geochemistry.).

Gass, I. G. (1958). Ultrabasic pillow lavas from Cyprus. *Geological Magazine*, *95*(3), 241–251. https://doi.org/10.1017/s0016756800066152

Gass, I. G., MacLeod, C. J., Murton, B. J., Panayiotou, A., Simonian, K. O., & Xenophontos, C. (1994). *The geology of the southern Troodos transform fault zone* (Vol. 9, p. 218). Geological Survey Department Cyprus, Ministry of Agriculture, Natural Resources and Environment, Memoir.

Geological Survey Department Cyprus. (1995). *Geological map of Cyprus*, scale 1:250,000. Ministry of Agriculture, Natural Resources and Environment, Government of Cyprus.

George, R. P. (1978). Structural petrology of the Olympus ultramafic complex in the Troodos ophiolite, Cyprus. *GSA Bulletin*, *89*(6), 845–865. https://doi.org/10.1130/0016-7606(1978)89<845:spotou>2.0.co;2

Ghiorso, M. S. (1997). Thermodynamic models of igneous processes. *Annual Review of Earth and Planetary Sciences*, *25*(1), 221–241. https://doi.org/10.1146/annurev.earth.25.1.221

Ghiorso, M. S., & Sack, R. O. (1995). Chemical mass transfer in magmatic processes IV. A revised and internally consistent thermodynamic model for the interpolation and extrapolation of liquid-solid equilibria in magmatic systems at elevated temperatures and pressures. *Contributions to Mineralogy and Petrology*, *119*(2–3), 197–212. https://doi.org/10.1007/bf00307281

Golowin, R., Portnyagin, M., Hoernle, K., Sobolev, A., Kuzmin, D., & Werner, R. (2017). The role and conditions of second-stage mantle melting in the generation of low-Ti tholeiites and boninites: The case of the Manihiki Plateau and the Troodos ophiolite. *Contributions to Mineralogy and Petrology*, *172*(11–12), 1–18. https://doi.org/10.1007/s00410-017-1424-3

Greenbaum, D. (1977). The chromitiferous rocks of the Troodos ophiolite complex, Cyprus. *Economic Geology*, *72*(7), 1175–1194. https://doi.org/10.2113/gsecongeo.72.7.1175

Grocke, S. B., Cottrell, E., Silva, S. D., & Kelley, K. A. (2016). The role of crustal and eruptive processes versus source variations in controlling the oxidation state of iron in Central Andean magmas. *Earth and Planetary Science Letters*, *440*, 92–104. https://doi.org/10.1016/j.epsl.2016.01.026

21699356, 2023, 4, Downloaded from https://agupubs.onlinelibrary.wiley.com/doi/10.1029/2022JB025008 by CAS - Chengdu Library, Wiley Online Library on [20/05/2024]. See the Terms and Conditions (https://onlinelibrary.wiley.com/terms-and-conditions) on Wiley Online Library for rules of use; OA articles are governed by the applicable Creative Commons License

Gualda, G. A. R., Ghiorso, M. S., Lemons, R. V., & Carley, T. L. (2012). Rhyolite-MELTS: A modified calibration of MELTS optimized for silica-rich, fluid-bearing magmatic systems. *Journal of Petrology*, *53*(5), 875–890. https://doi.org/10.1093/petrology/egr080

Hellebrand, E., Snow, J. E., Dick, H. J., & Hofmann, A. W. (2001). Coupled major and trace elements as indicators of the extent of melting in mid-ocean-ridge peridotites. *Nature*, *410*(6829), 677–681. https://doi.org/10.1038/35070546

Herd, C. D. K. (2008). Basalts as probes of planetary interior redox state. *Reviews in Mineralogy and Geochemistry*, *68*(1), 527–553. https://doi.org/10.2138/rmg.2008.68.19

Hu, W. J., Zhou, M. F., Malpas, J., & Ren, Z. Y. (2021). High-Ca boninitic melt inclusions in lavas of the Troodos ophiolite and a reappraisal of genetic relationships between different lava types. *GSA Bulletin*, *133*(9–10), 1831–1850. https://doi.org/10.1130/b35717.1

Ishizuka, O., Kimura, J. I., Li, Y. B., Stern, R. J., Reagan, M. K., Taylor, R. N., et al. (2006). Early stages in the evolution of Izu–Bonin arc volcanism: New age, chemical, and isotopic constraints. *Earth and Planetary Science Letters*, *250*(1–2), 385–401. https://doi.org/10.1016/j.epsl.2006.08.007

Ishizuka, O., Tani, K., & Reagan, M. K. (2014). Izu-Bonin-Mariana forearc crust as a modern ophiolite analogue. *Elements*, *10*(2), 115–120. https://doi.org/10.2113/gselements.10.2.115

Ishizuka, O., Tani, K., Reagan, M. K., Kanayama, K., Umino, S., Harigane, Y., et al. (2011). The timescales of subduction initiation and subsequent evolution of an oceanic island arc. *Earth and Planetary Science Letters*, *306*(3–4), 229–240. https://doi.org/10.1016/j.epsl.2011.04.006

Jenner, F. E., & O'Neill, H. S. C. (2012). Analysis of 60 elements in 616 ocean floor basaltic glasses. *Geochemistry, Geophysics, Geosystems*, *13*(2). https://doi.org/10.1029/2011gc004009

Johnson, M. C., & Plank, T. (1999). Dehydration and melting experiments constrain the fate of subducted sediments. *Geochemistry, Geophysics, Geosystems*, *1*(12). https://doi.org/10.1029/1999GC000014

Kelley, K. A., & Cottrell, E. (2009). Water and the oxidation state of subduction zone magmas. *Science*, *325*(5940), 605–607. https://doi.org/10.1126/science.1174156

Kelley, K. A., & Cottrell, E. (2012). The influence of magmatic differentiation on the oxidation state of Fe in a basaltic arc magma. *Earth and Planetary Science Letters*, *329*, 109–121. https://doi.org/10.1016/j.epsl.2012.02.010

Keppler, H. (1996). Constraints from partitioning experiments on the composition of subduction-zone fluids. *Nature*, *380*(6571), 237–240. https://doi.org/10.1038/380237a0

Kress, V. C., & Carmichael, I. S. E. (1991). The compressibility of silicate liquids containing Fe2O3 and the effect of composition, temperature, oxygen fugacity and pressure on their redox states. *Contributions to Mineralogy and Petrology*, *108*(1), 82–92. https://doi.org/10.1007/bf00307328

Le Bas, M. J. (2000). IUGS Reclassification of the high-Mg and picritic volcanic rocks. *Journal of Petrology*, *41*(10), 1467–1470. https://doi.org/10.1093/petrology/41.10.1467

Lee, C. T. A., Leeman, W. P., Canil, D., & Li, Z.-X. A. (2005). Similar V/Sc systematics in MORB and arc basalts: Implications for the oxygen fugacities of their mantle source regions. *Journal of Petrology*, *46*(11), 2313–2336. https://doi.org/10.1093/petrology/egi056

Lee, C. T. A., Luffi, P., Chin, E. J., Bouchet, R., Dasgupta, R., Morton, D. M., et al. (2012). Copper systematics in arc magmas and implications for crust mantle differentiation. *Science*, *336*(6077), 64–68. https://doi.org/10.1126/science.1217313

Lee, C. T. A., Luffi, P., Le Roux, V., Dasgupta, R., Albarede, F., & Leeman, W. P. (2010). The redox state of arc mantle using Zn/Fe systematics. *Nature*, *468*(7324), 681–685. https://doi.org/10.1038/nature09617

Lee, C. T. A., & Tang, M. (2020). How to make porphyry copper deposits. *Earth and Planetary Science Letters*, *529*, 115868. https://doi.org/10.1016/j.epsl.2019.115868

Le Roux, V., Dasgupta, R., & Lee, C. T. A. (2015). Recommended mineral-melt partition coefficients for FRTEs (Cu), Ga, and Ge during mantle melting. *American Mineralogist*, *100*(11–12), 2533–2544. https://doi.org/10.2138/am-2015-5215

Li, H. Y., Taylor, R. N., Prytulak, J., Kirchenbaur, M., Shervais, J. W., Ryan, J. G., et al. (2019). Radiogenic isotopes document the start of subduction in the Western Pacific. *Earth and Planetary Science Letters*, *518*, 197–210. https://doi.org/10.1016/j.epsl.2019.04.041

Li, J. L., Schwarzenbach, E. M., John, T., Ague, J. J., Huang, F., Gao, J., et al. (2020). Uncovering and quantifying the subduction zone sulfur cycle from the slab perspective. *Nature Communications*, *11*(1), 514. https://doi.org/10.1038/s41467-019-14110-4

Li, J. P., Kornprobst, J., Vielzeuf, D., & Fabriès, J. (1995). An improved experimental calibration of the olivine-spinel geothermometer. *Chinese Journal of Geochemistry*, *14*(1), 68–77. https://doi.org/10.1007/bf02840385

Li, Q. W., Nebel-Jacobsen, Y., Zhao, J. H., Nebel, O., Richter, M., Cawood, P. A., & Wang, Q. (2021). An early garnet redox-filter as an additive oxidizer in lower continental arc crust traced through Fe isotopes. *Journal of Geophysical Research: Solid Earth*, *126*(7), e2020JB021217. https://doi.org/10.1029/2020jb021217

Li, X. H., Li, W. X., Li, Q. L., Wang, X. C., Liu, Y., & Yang, Y. H. (2010). Petrogenesis and tectonic significance of the ~850 Ma Gangbian alkaline complex in South China: Evidence from in situ zircon U–Pb dating, Hf–O isotopes and whole-rock geochemistry. *Lithos*, *114*(1–2), 1–15. https://doi.org/10.1016/j.lithos.2009.07.011

Liu, Y., Hu, Z., Gao, S., Günther, D., Xu, J., Gao, C., & Chen, H. (2008). In situ analysis of major and trace elements of anhydrous minerals by LA-ICP-MS without applying an internal standard. *Chemical Geology*, *257*(1–2), 34–43. https://doi.org/10.1016/j.chemgeo.2008.08.004

Ludwig, K. R. (2003). *User manual for Isoplot 3.0* (Vol. 4). Berkeley Geochronology Center Special Publication.

Mallmann, G., & O'Neill, H. S. C. (2009). The crystal/melt partitioning of V during mantle melting as a function of oxygen fugacity compared with some other elements (Al, P, Ca, Sc, Ti, Cr, Fe, Ga, Y, Zr and Nb). *Journal of Petrology*, *50*(9), 1765–1794. https://doi.org/10.1093/petrology/egp053

Malpas, J. (1990). Crustal accretionary processes in the Troodos ophiolite, Cyprus: Evidence from field mapping and deep crustal drilling. In J. Malpas, E. M. Moores, A. Panayiotou, & C. Xenophontos (Eds.), *Ophiolites: Oceanic crustal analogues* (pp. 65–74). Cyprus Geological Survey Department.

Malpas, J., & Langdon, G. (1984). Petrology of the upper pillow lava suite, Troodos ophiolite, Cyprus. *Geological Society, London, Special Publications*, *13*, 155–167. https://doi.org/10.1144/GSL.SP.1984.013.01.14

Mattioli, G. S., & Wood, B. J. (1988). Magnetite activities across the MgAl2O4-Fe3O4 spinel join, with application to thermobarometric estimates of upper mantle oxygen fugacity. *Contributions to Mineralogy and Petrology*, *98*(2), 148–162. https://doi.org/10.1007/bf00402108

Miyashiro, A. (1973). The Troodos ophiolitic complex was probably formed in an island arc. *Earth and Planetary Science Letters*, *19*(2), 218–224. https://doi.org/10.1016/0012-821x(73)90118-0

Moussallam, Y., Edmonds, M., Scaillet, B., Peters, N., Gennaro, E., Sides, I., & Oppenheimer, C. (2016). The impact of degassing on the oxidation state of basaltic magmas: A case study of Kīlauea volcano. *Earth and Planetary Science Letters*, *450*, 317–325. https://doi.org/10.1016/j.epsl.2016.06.031

Moussallam, Y., Longpré, M. A., McCammon, C., Gomez-Ulla, A., Rose-Koga, E. F., Scaillet, B., et al. (2019). Mantle plumes are oxidised. *Earth and Planetary Science Letters*, *527*, 115798. https://doi.org/10.1016/j.epsl.2019.115798

21699356, 2023, 4, Downloaded from https://agupubs.onlinelibrary.wiley.com/doi/10.1029/2022JB025008 by CAS - Chengdu Library, Wiley Online Library on [20/05/2024]. See the Terms and Conditions (https://onlinelibrary.wiley.com/terms-and-conditions) on Wiley Online Library for rules of use; OA articles are governed by the applicable Creative Commons License

Moussallam, Y., Oppenheimer, C., Scaillet, B., Gaillard, F., Kyle, P., Peters, N., et al. (2014). Tracking the changing oxidation state of Erebus magmas, from mantle to surface, driven by magma ascent and degassing. *Earth and Planetary Science Letters*, *393*, 200–209. https://doi.org/10.1016/j.epsl.2014.02.055

Mukasa, S. B., & Ludden, J. N. (1987). Uranium-lead isotopic ages of plagiogranites from the Troodos ophiolite, Cyprus, and their tectonic significance. *Geology*, *15*(9), 825–828. https://doi.org/10.1130/0091-7613(1987)15<825:uiaopf>2.0.co;2

Murton, B. J. (1989). Tectonic controls on boninite genesis. *Geological Society, London, Special Publications*, *42*(1), 347–377. https://doi.org/10.1144/gsl.sp.1989.042.01.20

Muth, M. J., & Wallace, P. J. (2021). Slab-derived sulfate generates oxidized basaltic magmas in the southern Cascade arc (California, USA). *Geology*, *49*(10), 1177–1181. https://doi.org/10.1130/g48759.1

Nicholls, J., Carmichael, I. S. E., & Stormer, J. C. (1971). Silica activity and P total in igneous rocks. *Contributions to Mineralogy and Petrology*, *33*(1), 1–20. https://doi.org/10.1007/bf00373791

Nicklas, R. W., Hahn, R. K., Willhite, L. N., Jackson, M. G., Zanon, V., Arevalo, R., Jr., & Day, J. M. (2022). Oxidized mantle sources of HIMU- and EM-type Ocean Island Basalts. *Chemical Geology*, *602*, 120901. https://doi.org/10.1016/j.chemgeo.2022.120901

Nicklas, R. W., Puchtel, I. S., & Ash, R. D. (2018). Redox state of the Archean mantle: Evidence from V partitioning in 3.5–2.4 Ga komatiites. *Geochimica et Cosmochimica Acta*, *222*, 447–466. https://doi.org/10.1016/j.gca.2017.11.002

Nikolaev, G. S., Ariskin, A. A., Barmina, G. S., Nazarov, M. A., & Almeev, R. R. (2016). Test of the Ballhaus–Berry–Green Ol–Opx–Sp oxybarometer and calibration of a new equation for estimating the redox state of melts saturated with olivine and spinel. *Geochemistry International*, *54*(4), 301–320. https://doi.org/10.1134/s0016702916040078

O'Neill, H. S. (1987). Quartz-fayalite-iron and quartz-fayalite-magnetite equilibria and the free energy of formation of fayalite (Fe2SiO4) and magnetite (Fe3O4). *American Mineralogist*, *72*(1–2), 67–75.

O'Neill, H. S. C., & Wall, V. J. (1987). The Olivine-Orthopyroxene-Spinel oxygen geobarometer, the nickel precipitation curve, and the oxygen fugacity of the Earth's Upper Mantle. *Journal of Petrology*, *28*(6), 1169–1191. https://doi.org/10.1093/petrology/28.6.1169

Osozawa, S., Shinjo, R., Lo, C. H., Jahn, B. M., Hoang, N., Sasaki, M., et al. (2012). Geochemistry and geochronology of the Troodos ophiolite: An SSZ ophiolite generated by subduction initiation and an extended episode of ridge subduction? *Lithosphere*, *4*(6), 497–510. https://doi.org/10.1130/l205.1

Parkinson, I. J., & Arculus, R. J. (1999). The redox state of subduction zones: Insights from arc-peridotites. *Chemical Geology*, *160*(4), 409–423. https://doi.org/10.1016/s0009-2541(99)00110-2

Parkinson, I. J., Arculus, R. J., & Eggins, S. M. (2003). Peridotite xenoliths from Grenada, lesser Antilles island arc. *Contributions to Mineralogy and Petrology*, *146*(2), 241–262. https://doi.org/10.1007/s00410-003-0500-z

Parkinson, I. J., & Pearce, J. A. (1998). Peridotites from the Izu–Bonin–Mariana forearc (ODP Leg 125): Evidence for mantle melting and melt–mantle interaction in a supra-subduction zone setting. *Journal of Petrology*, *39*(9), 1577–1618. https://doi.org/10.1093/petroj/39.9.1577

Parman, S. W., & Grove, T. L. (2004). Harzburgite melting with and without H2O: Experimental data and predictive modeling. *Journal of Geophysical Research: Solid Earth*, *109*(B2). https://doi.org/10.1029/2003jb002566

Pearce, J. A., Barker, P. F., Edwards, S. J., Parkinson, I. J., & Leat, P. T. (2000). Geochemistry and tectonic significance of peridotites from the South Sandwich arc–basin system, South Atlantic. *Contributions to Mineralogy and Petrology*, *139*(1), 36–53. https://doi.org/10.1007/s004100050572

Pearce, J. A., & Reagan, M. K. (2019). Identification, classification, & interpretation of boninites from Anthropocene to Eoarchean using Si-Mg-Ti systematics. *Geosphere*, *15*(4), 1008–1037. https://doi.org/10.1130/ges01661.1

Pearce, J. A., & Robinson, P. T. (2010). The Troodos ophiolitic complex probably formed in a subduction initiation, slab edge setting. *Gondwana Research*, *18*(1), 60–81. https://doi.org/10.1016/j.gr.2009.12.003

Pearce, J. A., Stern, R. J., Bloomer, S. H., & Fryer, P. (2005). Geochemical mapping of the Mariana arc-basin system: Implications for the nature and distribution of subduction components. *Geochemistry, Geophysics, Geosystems*, *6*(7), Q07006. https://doi.org/10.01029/02004GC000895

Pearce, J. A., Thirlwall, M. F., Ingram, G., Murton, B. J., Arculus, R. J., & Van der Laan, S. R. (1992). Isotopic evidence for the origin of boninites and related rocks drilled in the Izu-Bonin (Ogasawara) forearc, Leg 125. In P. Fryer, J. A. Pearce, L. Stokking, et al. (Eds.), *Proceedings of the ocean drilling program, scientific results 125*, Texas A&M University, 125 (pp. 237–261). IODP.

Piccoli, F., Hermann, J., Pettke, T., Connolly, J. A. D., Kempf, E. D., & Vieira Duarte, J. F. (2019). Subducting serpentinites release reduced, not oxidized, aqueous fluids. *Scientific Reports*, *9*(1), 1–7. https://doi.org/10.1038/s41598-019-55944-8

Portnyagin, M. V., Danyushevsky, L. V., & Kamenetsky, V. S. (1997). Coexistence of two distinct mantle sources during formation of ophiolites: A case study of primitive pillow-lavas from the lowest part of the volcanic section of the Troodos Ophiolite, Cyprus. *Contributions to Mineralogy and Petrology*, *128*(2–3), 287–301. https://doi.org/10.1007/s004100050309

Portnyagin, M. V., Magakyan, R., & Schmincke, H.-U. (1996). Geochemical variability of boninite magmas: Evidence from magmatic inclusions in highly magnesian olivine from lavas of southwestern Cyprus. *Petrology*, *4*, 231–246.

Putirka, K. D., Perfit, M., Ryerson, F. J., & Jackson, M. G. (2007). Ambient and excess mantle temperatures, olivine thermometry, and active vs. passive upwelling. *Chemical Geology*, *241*(3–4), 177–206. https://doi.org/10.1016/j.chemgeo.2007.01.014

Reagan, M. K., Heaton, D. E., Schmitz, M. D., Pearce, J. A., Shervais, J. W., & Koppers, A. A. P. (2019). Forearc ages reveal extensive short-lived & rapid seafloor spreading following subduction initiation. *Earth and Planetary Science Letters*, *506*, 520–529. https://doi.org/10.1016/j.epsl.2018.11.020

Reagan, M. K., Ishizuka, O., Stern, R. J., Kelley, K. A., Ohara, Y., Blichert-Toft, J., et al. (2010). Fore-arc basalts & subduction initiation in the Izu-Bonin-Mariana system. *Geochemistry, Geophysics, Geosystems*, *11*, Q03X12. https://doi.org/10.1029/2009GC002871

Reagan, M. K., Pearce, J. A., Petronotis, K., Almeev, R. R., Avery, A. J., Carvallo, C., et al. (2017). Subduction initiation and ophiolite crust: New insights from IODP drilling. *International Geology Review*, *59*(11), 1439–1450. https://doi.org/10.1080/00206814.2016.1276482

Regelous, M., Haase, K. M., Freund, S., Keith, M., Weinzierl, C. G., Beier, C., et al. (2014). Formation of the Troodos Ophiolite at a triple junction: Evidence from trace elements in volcanic glass. *Chemical Geology*, *386*, 66–79. https://doi.org/10.1016/j.chemgeo.2014.08.006

Ribeiro, J. M., & Lee, C. T. A. (2017). An imbalance in the deep water cycle at subduction zones: The potential importance of the fore-arc mantle. *Earth and Planetary Science Letters*, *479*, 298–309. https://doi.org/10.1016/j.epsl.2017.09.018

Ribeiro, J. M., MacLeod, C., Lissenberg, J., Ryan, J., & Macpherson, C. (2022). Origin and evolution of the slab fluids since subduction inception in the Izu-Bonin-Mariana: A comparison with the southeast Mariana fore-arc rift. *Chemical Geology*, *601*, 120813. https://doi.org/10.1016/j.chemgeo.2022.120813

Ribeiro, J. M., Stern, R. J., Kelley, K. A., Shaw, A. M., Martinez, F., & Ohara, Y. (2015). Composition of the slab-derived fluids released beneath the Mariana forearc: Evidence for shallow dehydration of the subducting plate. *Earth and Planetary Science Letters*, *418*, 136–148. https://doi.org/10.1016/j.epsl.2015.02.018

21699356, 2023, 4, Downloaded from https://agupubs.onlinelibrary.wiley.com/doi/10.1029/2022JB025008 by CAS - Chengdu Library, Wiley Online Library on [20/05/2024]. See the Terms and Conditions (https://onlinelibrary.wiley.com/terms-and-conditions) on Wiley Online Library for rules of use; OA articles are governed by the applicable Creative Commons License

Robertson, A., & Xenophontos, C. (1993). Development of concepts concerning the Troodos ophiolite and adjacent units in Cyprus. *Geological Society, London, Special Publications*, *76*(1), 85–119. https://doi.org/10.1144/gsl.sp.1993.076.01.05

Robinson, P. T., Melson, W. G., O'Hearn, T., & Schmincke, H. U. (1983). Volcanic glass compositions of the Troodos ophiolite, Cyprus. *Geology*, *11*(7), 400–404. https://doi.org/10.1130/0091-7613(1983)11<400:vgcott>2.0.co;2

Rogers, N. W., MacLeod, C. J., & Murton, B. J. (1989). Petrogenesis of boninitic lavas from the Limassol Forrest complex. In A. J. Crawford (Ed.), *Boninites and related rocks* (pp. 289–313). Unwin-Hyman.

Ryerson, F. J., & Watson, E. B. (1987). Rutile saturation in magmas: Implications for Ti-Nb-Ta depletion in island arc basalts. *Earth and Planetary Science Letters*, *86*(2–4), 225–239. https://doi.org/10.1016/0012-821x(87)90223-8

Schuiling, R. D. (2011). Troodos: A giant serpentinite diapir. *International Journal of Geosciences*, *2*(2), 98–101. https://doi.org/10.4236/ijg.2011.22010

Shervais, J. W., Reagan, M., Haugen, E., Almeev, R. R., Pearce, J. A., Prytulak, J., et al. (2019). Magmatic response to subduction initiation: Part 1. fore-arc basalts of the Izu-Bonin arc from IODP Expedition 352. *Geochemistry, Geophysics, Geosystems*, *20*(1), 314–338. https://doi.org/10.1029/2018gc007731

Shervais, J. W., Reagan, M. K., Godard, M., Prytulak, J., Ryan, J. G., Pearce, J. A., et al. (2021). Magmatic response to subduction initiation, Part II: Boninites and related rocks of the Izu-Bonin arc from IOPD Expedition 352. *Geochemistry, Geophysics, Geosystems*, *22*(1), e2020GC009093. https://doi.org/10.1029/2020GC009093

Simonian, K. T., & Gass, I. G. (1978). Arakapas fault belt, Cyprus: A fossil transform fault. *GSA Bulletin*, *89*(8), 1220–1230. https://doi.org/10.1130/0016-7606(1978)89<1220:afbcaf>2.0.co;2

Smith, P. M., & Asimow, P. D. (2005). Adiabat_1ph: A new public front-end to the MELTS, pMELTS, and pHMELTS models. *Geochemistry, Geophysics, Geosystems*, *6*(2). https://doi.org/10.1029/2004gc000816

Sobolev, A. V., & Chaussidon, M. (1996). H_2O concentrations in primary melts from supra-subduction zones and mid-ocean ridges: Implications for H_2O storage and recycling in the mantle. *Earth and Planetary Science Letters*, *137*(1–4), 45–55. https://doi.org/10.1016/0012-821x(95)00203-o

Sobolev, A. V., Dmitriev, L. V., Tsameryan, O. P., Kononkova, N. N., & Robinson, P. T. (1991). A possible primary melt composition for the ultramafic lavas of the Margi area, Troodos Ophiolite. In I. L. Gibson, J. Malpas, P. T. Robinson, & C. Xenophontos (Eds.), *Cyprus crustal study project initial report, holes CY-1 and 1a* (pp. 203–216). Geological Survey of Canada

Stern, R. J., Reagan, M., Ishizuka, O., Ohara, Y., & Whattam, S. (2012). To understand subduction initiation, study forearc crust: To understand forearc crust, study ophiolites. *Lithosphere*, *4*(6), 469–483. https://doi.org/10.1130/l183.1

Sun, S.-S., & McDonough, W. F. (1989). Chemical and isotopic systematics of oceanic basalts: Implications for mantle composition and processes. In A. D. Saunders & M. J. Norry (Eds.), *Magmatism in the ocean basins* (Vol. 42, pp. 313–345). Geological Society, London, Special Publications.

Tang, M., Erdman, M., Eldridge, G., & Lee, C.-T. A. (2018). The redox "filter" beneath magmatic orogens and the formation of continental crust. *Science Advances*, *4*(5). https://doi.org/10.1126/sciadv.aar4444

Tomkins, A. G., & Evans, K. A. (2015). Separate zones of sulfate and sulfide release from subducted mafic oceanic crust. *Earth and Planetary Science Letters*, *428*, 73–83. https://doi.org/10.1016/j.epsl.2015.07.028

Umino, S., Kitamura, K., Kanayama, K., Tamura, A., Sakamoto, N., Ishizuka, O., & Arai, S. (2015). Thermal and chemical evolution of the subarc mantle revealed by spinel-hosted melt inclusions in boninite from the Ogasawara (Bonin) Archipelago, Japan. *Geology*, *43*(2), 151–154. https://doi.org/10.1130/g36191.1

Warren, J. M. (2016). Global variations in abyssal peridotite compositions. *Lithos*, *248*, 193–219. https://doi.org/10.1016/j.lithos.2015.12.023

Wasylenki, L. E., Baker, M. B., Kent, A. J. R., & Stolper, E. M. (2003). Near-solidus melting of the shallow upper mantle: Partial melting experiments on depleted peridotite. *Journal of Petrology*, *44*(7), 1163–1191. https://doi.org/10.1093/petrology/44.7.1163

Wilson, R. A. M. (1959). *The geology of the Xeros-Troodos area*. Ministry of Agriculture & Natural Resources, Geological Survey Department.

Woelki, D., Michael, P. J., Regelous, M., & Haase, K. M. (2020). Enrichment of H2O and fluid-soluble trace elements in the Troodos a far Ophiolite: Evidence for a near trench origin. *Lithos*, *356*, 105299. https://doi.org/10.1016/j.lithos.2019.105299

Woelki, D., Regelous, M., Haase, K. M., & Beier, C. (2019). Geochemical mapping of a paleo-subduction zone beneath the Troodos Ophiolite. *Chemical Geology*, *523*, 1–8. https://doi.org/10.1016/j.chemgeo.2019.05.041

Woelki, D., Regelous, M., Haase, K. M., Romer, R. H. W., & Beier, C. (2018). Petrogenesis of boninitic lavas from the Troodos Ophiolite, and comparison with Izu-Bonin-Mariana fore-arc crust. *Earth and Planetary Science Letters*, *498*, 203–214. https://doi.org/10.1016/j.epsl.2018.06.041

Wood, B. J., Bryndzia, L. T., & Johnson, K. E. (1990). Mantle oxidation-state and its relationship to tectonic environment and fluid speciation. *Science*, *248*(4953), 337–345. https://doi.org/10.1126/science.248.4953.337

Wood, B. J., & Turner, S. P. (2009). Origin of primitive high-Mg andesite: Constraints from natural examples & experiments. *Earth and Planetary Science Letters*, *283*(1–4), 59–66. https://doi.org/10.1016/j.epsl.2009.03.032

Wood, B. J., & Virgo, D. (1989). Upper mantle oxidation state: Ferric iron contents of lherzolite spinels by ^{57}Mössbauer spectroscopy & resultant oxygen fugacities. *Geochimica et Cosmochimica Acta*, *53*, 1277–1291.

Woodland, A. B., Kornprobst, J., McPherson, E., Bodinier, J. L., & Menzies, M. A. (1996). Metasomatic interactions in the lithospheric mantle: Petrologic evidence from the Lherz Massif, French Pyrenees. *Chemical Geology*, *134*(1–3), 83–112. https://doi.org/10.1016/s0009-2541(96)00082-4

Workman, R. K., & Hart, S. R. (2005). Major and trace element composition of the depleted MORB mantle (DMM). *Earth and Planetary Science Letters*, *231*(1–2), 53–72. https://doi.org/10.1016/j.epsl.2004.12.005

Zhang, H. L., Hirschmann, M. M., Cottrell, E., & Withers, A. C. (2017). Effect of pressure on $Fe^{3+}/\Sigma Fe$ ratio in a mafic magma and consequences for magma ocean redox gradients. *Geochimica et Cosmochimica Acta*, *204*, 83–103. https://doi.org/10.1016/j.gca.2017.01.023

Zhang, P. F., Uysal, I., Zhou, M. F., Su, B. X., & Avcı, E. (2016). Subduction initiation for the formation of high-Cr chromitites in the Kop ophiolite, NE Turkey. *Lithos*, *260*(s1), 345–355. https://doi.org/10.1111/1755-6724.13006

Zhang, P. F., Zhou, M. F., Malpas, J., & Robinson, P. T. (2020). Origin of high-Cr chromite deposits in nascent mantle wedges: Petrological and geochemical constraints from the neo-Tethyan Luobusa ophiolite, Tibet. *Ore Geology Reviews*, *123*, 103581. https://doi.org/10.1016/j.oregeorev.2020.103581

Zhou, M. F., Robinson, P. T., & Bai, W. J. (1994). Formation of podiform chromitites by melt/rock interaction in the upper mantle. *Mineralium Deposita*, *29*(1), 98–101. https://doi.org/10.1007/bf03326400

Zhou, M. F., Robinson, P. T., Su, B. X., Gao, J. F., Li, J. W., Yang, J. S., & Malpas, J. (2014). Compositions of chromite, associated minerals, and parental magmas of podiform chromite deposits: The role of slab contamination of asthenospheric melts in suprasubduction zone environments. *Gondwana Research*, *26*(1), 262–283. https://doi.org/10.1016/j.gr.2013.12.011

21699356, 2023, 4, Downloaded from https://agupubs.onlinelibrary.wiley.com/doi/10.1029/2022JB025008 by CAS - Chengdu Library, Wiley Online Library on [20/05/2024]. See the Terms and Conditions (https://onlinelibrary.wiley.com/terms-and-conditions) on Wiley Online Library for rules of use; OA articles are governed by the applicable Creative Commons License

Zhou, M. F., Sun, M., Keays, R. R., & Kerrich, R. W. (1998). Controls on platinum-group elemental distributions of podiform chromitites: A case study of high-Cr and high-Al chromitites from Chinese orogenic belts. *Geochimica et Cosmochimica Acta*, *62*(4), 677–688. https://doi.org/10.1016/s0016-7037(97)00382-7

Zhou, X., Li, Z. H., Gerya, T. V., Stern, R. J., Xu, Z., & Zhang, J. (2018). Subduction initiation dynamics along a transform fault control trench curvature and ophiolite ages. *Geology*, *46*(7), 607–610. https://doi.org/10.1130/g40154.1

References From the Supporting Information

Wan, Z., Coogan, L. A., & Dante, C. (2008). Experimental calibration of aluminum partitioning between olivine and spinel as a geothermometer. *American Mineralogist*, *93*(7), 1142–1147. https://doi.org/10.2138/am.2008.2758

21699356, 2023, 4, Downloaded from https://agupubs.onlinelibrary.wiley.com/doi/10.1029/2022JB025008 by CAS - Chengdu Library, Wiley Online Library on [20/05/2024]. See the Terms and Conditions (https://onlinelibrary.wiley.com/terms-and-conditions) on Wiley Online Library for rules of use; OA articles are governed by the applicable Creative Commons License